

This Work has been submitted to the Journal of Atmospheric Sciences. Copyright in this Work may be transferred without further notice.

MS-GWaM: A 3-dimensional transient gravity wave parametrization for atmospheric models

Georg S. Voelker^a, Gergely Bölöni^b, Young-Ha Kim^a, Günther Zängl^b,
and Ulrich Achatz^a

^a *Institute for Atmosphere and Environment, Goethe University Frankfurt, Frankfurt, Germany*

^b *Deutscher Wetterdienst, Offenbach am Main, Germany*

arXiv:2309.11257v2 [physics.flu-dyn] 27 Feb 2024

Corresponding author: Georg S. Voelker, voelker@iau.uni-frankfurt.de

ABSTRACT: Parametrizations for internal gravity waves in atmospheric models are traditionally subject to a number of simplifications. Most notably, they rely on both neglecting wave propagation and advection in the horizontal direction (single-column assumption) and an instantaneous balance in the vertical direction (steady-state assumption). While these simplifications are well justified to cover some essential dynamic effects and keep the computational effort small it has been shown that both mechanisms are potentially significant. In particular, the recently introduced Multiscale Gravity Wave Model (MS-GWaM) successfully applied ray tracing methods in a novel type of transient but columnar internal gravity wave parameterization (MS-GWaM-1D). We extend this concept to a three-dimensional version of the parameterization (MS-GWaM-3D) to simulate subgrid-scale non-orographic internal gravity waves. The resulting global wave model—implemented into the weather-forecast and climate code ICON—contains three-dimensional transient propagation with accurate flux calculations, a latitude-dependent background source, and convectively generated waves. MS-GWaM-3D helps reproducing expected temperature and wind patterns in the mesopause region in the climatological zonal mean state and thus proves a viable IGW parameterization. Analyzing the global wave action budget, we find that horizontal wave propagation is as important as vertical wave propagation. The corresponding wave refraction includes previously missing but well-known effects such as wave refraction into the polar jet streams. On a global scale, three-dimensional wave refraction leads to a horizontal flow-dependent redistribution of waves such that the structures of the zonal mean wave drag and consequently the zonal mean winds are modified.

1. Introduction

Internal gravity waves (IGWs) play a significant role in distributing energy and momentum throughout the atmosphere. Being generated through the perturbation of balanced flow states in stratified environments (e.g. convection, flow over topography, flow instabilities, wave turbulence, etc.) they may propagate over large distances and deposit their energy, generate turbulence and modify the mean-flow dynamics in general far away from their source (Fritts and Alexander 2003; Alexander et al. 2010; Sutherland 2010; Nappo 2013; Williams et al. 2017; Sutherland et al. 2019; Achatz 2022). While propagating, they may exchange energy among themselves, transiently interact with mean flows, or influence the transport of chemical species. Even though their generation regions are mostly located in the troposphere, their effects are strongest in the middle atmosphere (Lindzen 1981; Kim et al. 2003; Sigmond and Scinocca 2010). However, these major effects may couple to and thus impact for instance tropospheric weather patterns or climate conditions (Scaife et al. 2005, 2012; Sigmond and Scinocca 2010).

In state-of-the-art general circulation models (GCMs) or numerical weather prediction (NWP) models, gravity waves are only partially resolved and thus need parameterization (e.g. Kim et al. 2003; Holt et al. 2016). Even when entering the global kilometer-resolving regime, their effects are not entirely represented (Kruse et al. 2022; Polichtchouk et al. 2022, 2023). IGW parameterizations commonly rely on WKBJ theories (Bretherton 1966; Grimshaw 1975; Achatz et al. 2017), incorporating some major simplifications (Lindzen 1981; Medvedev and Klaassen 1995; Warner and McIntyre 1996; Hines 1997b,a; Lott and Miller 1997; Alexander and Dunkerton 1999; Scinocca 2003; Orr et al. 2010; Lott and Guez 2013). Most notably, there are three assumptions that are usually made and shall be considered in this work. Firstly, local horizontal homogeneity is assumed in the so-called single-column approximation, i.e. horizontal gradients of the resolved flow are neglected, which leads horizontal wave numbers to be invariant during propagation. Furthermore, responses of the resolved flow due to the horizontal finiteness of an IGW field are neglected. Secondly, a steady-state assumption is adopted such that IGWs instantly propagate through the atmosphere, leading to a neglect of all transient propagation effects. Thirdly, it is commonly assumed that the resolved flow is (approximately) in hydrostatic and geostrophic balance, implying a reduced formula for the resolved-flow response to IGWs. In the extratropics, this can lead to significant modifications in the IGW forcing when the flow is imbalanced.

Recent investigations suggested^{GSV} that the mentioned effects can have important impacts on modeled flows (Sato et al. 2009; Bölöni et al. 2016; Ehard et al. 2017; Wei et al. 2019). In particular, Bölöni et al. (2016) showed, that including the time dependence of the gravity wave propagation significantly improves the estimated wave drag in idealized simulations. Sato et al. (2009) found that three-dimensional propagation pathways can impact the structure of the stratosphere and mesosphere using wave resolving general circulation models. Similarly, Ehard et al. (2017) highlight the importance of horizontal gravity wave propagation for the dynamics of the Antarctic polar night jet by analyzing various observations and reanalyses. Finally, Wei et al. (2019) showed that describing the wave momentum fluxes with a direct formulation can improve the simulated wave impact on the resolved flow.^{GSV} Several studies have successfully relaxed some of the simplifications in model parameterizations^{GSV} (e.g. Muraschko et al. 2015; Wilhelm et al. 2018; Quinn et al. 2020). In particular, Bölöni et al. (2021) and Kim et al. (2021) presented a novel Lagrangian IGW parameterization, the Multi-Scale Gravity-Wave Model (MS-GWaM). It is built on a weakly non-linear WKB theory, including transient wave-mean flow interactions. The model has been implemented in a single-column mode into a state-of-the-art weather forecast and climate code. It will therefore be referred to as MS-GWaM-1D throughout this manuscript. Here, we present MS-GWaM-3D, an extension of MS-GWaM-1D, which models the full 3D transient propagation of IGWs and their forcing of the general (cf. balanced) resolved flow. While both the columnar approximation and assumptions on the resolved flow are relaxed in MS-GWaM-3D, we shall focus on the effects of the horizontal propagation in this study. In particular, the modified refraction behavior and resolved flow response in the statistical mean are investigated. Indeed we find that many aspects show an increased realism of the wave dynamics. However, our results also underline the challenges left for future studies.^{GSV} Ultimately, we aim to improve the representation of the parameterized IGW processes while keeping simulations numerically efficient.

This paper is structured as follows. First, a brief recapitulation of the underlying WKB theory for transient, 3-dimensional IGWs (Sec. 2) is presented. It is then followed by the description of the employed ray tracing techniques (Sec. 3). Lastly, results from simulations with MS-GWaM-3D (Sec. 4) are visualized and discussed. The manuscript then closes with some concluding remarks on the achievements and challenges of ray tracing parameterization (Sec. 5).

2. Nonlinear, 3-dimensional and transient internal gravity waves

Albeit generally 3-dimensional and transient, internal gravity waves are commonly parameterized using both the single-column and the steady-state approximations. Here, we attempt to relax both these assumptions and build a 3-dimensional and transient parameterization. An underlying multiscale theory has been presented by Achatz et al. (2010, 2017, 2023) and thus we restrict ourselves to summarizing the results here for brevity.^{GSV}

a. Wave evolution

We follow the analysis of Bretherton (1966); Grimshaw (1974); Hasha et al. (2008); Achatz et al. (2017); Achatz (2022); Achatz et al. (2023) and summarize the Bretherton-Grimshaw modulation equations for a quasi-monochromatic wave train on a sphere. In particular the wave and mean-flow dynamics are derived by means of a WKBJ expansion of the compressible Euler equations. We extend the existing theories by^{GSV} the inclusion of the atmospheric density scale height to improve the realism in the non-hydrostatic regime. Most notably, the scale height correction plays an important role in the course of vertical wave reflection, where vertical wave numbers become small with respect to the inverse scale height, Γ . We then arrive at the^{GSV} well-known dispersion relation,

$$\begin{aligned}\omega(\mathbf{r}, t) &= \Omega(\mathbf{r}, t, \mathbf{k}) \\ &= \mathbf{k} \cdot \mathbf{U} \pm \sqrt{\frac{f^2(k_r^2 + \Gamma^2) + N^2(k_\lambda^2 + k_\phi^2)}{K^2}},\end{aligned}\tag{1}$$

with the position vector, $\mathbf{r} = \lambda \mathbf{e}_\lambda + \phi \mathbf{e}_\phi + r \mathbf{e}_r$, and the wave vector, $\mathbf{k} = k_\lambda \mathbf{e}_\lambda + k_\phi \mathbf{e}_\phi + k_r \mathbf{e}_r$. Here λ , ϕ and r are the standard geographical spherical coordinates, and \mathbf{e}_λ , \mathbf{e}_ϕ and \mathbf{e}_r are the corresponding unit vectors. Note that the mean-flow velocity $\mathbf{U}(\mathbf{r}, t) = U \mathbf{e}_\lambda + V \mathbf{e}_\phi$, the Coriolis frequency, $f = f(\mathbf{r})$, and the buoyancy frequency, $N = N(\mathbf{r}, t)$, are functions of space and time as indicated. For convenience, we have defined the total wave vector squared as $K^2 = \mathbf{k} \cdot \mathbf{k} + \Gamma^2$, with the scale height correction $\Gamma = \Gamma(\mathbf{r}, t)$. Finally, we would like the reader to note that the theory is written in spherical coordinates. The corresponding eikonal equations and the group velocities, \mathbf{c}_g , for an

individual wave component then follow the relations

$$(\partial_t + \mathbf{c}_g \cdot \nabla_r) \mathbf{k} = \dot{\mathbf{k}} = -\nabla_r \Omega, \quad \mathbf{c}_g = \nabla_k \Omega. \quad (2)$$

Here we denote the gradients with respect to position and wave number by ∇_r and ∇_k , respectively. Having the application to a ray tracing scheme in mind, we indicate by a dot the derivative along characteristics, so-called rays, with their positions denoted by $\mathbf{r}(t)$ so that

$$\dot{\mathbf{r}} = \mathbf{c}_g. \quad (3)$$

Rays follow the local group velocity, and hence the propagation of wave energy. In particular, the prognostic equations for the zonal, meridional, and radial wave numbers, (k_λ, k_ϕ, k_r) , in spherical coordinates read

$$\dot{k}_\lambda = -\frac{1}{r \cos \phi} \left(\mathbf{k} \cdot \partial_\lambda \mathbf{U} + \frac{|\mathbf{k}_h|^2}{2\hat{\omega}K^2} \left[\partial_\lambda N^2 - \frac{N^2 - f^2}{K^2} \partial_\lambda \Gamma^2 \right] \right) - \frac{k_\lambda}{r} c_{gr} + \frac{k_\lambda \tan \phi}{r} c_{g\phi}, \quad (4)$$

$$\dot{k}_\phi = -\frac{1}{r} \left(\mathbf{k} \cdot \partial_\phi \mathbf{U} + \frac{|\mathbf{k}_h|^2}{2\hat{\omega}K^2} \left[\partial_\phi N^2 + \frac{k_r^2 + \Gamma^2}{|\mathbf{k}_h|^2} \partial_\phi f^2 - \frac{N^2 - f^2}{K^2} \partial_\phi \Gamma^2 \right] \right) - \frac{k_\phi}{r} c_{gr} - \frac{k_\lambda \tan \phi}{r} c_{g\lambda}, \quad (5)$$

$$\dot{k}_r = -\left(\mathbf{k} \cdot \partial_r \mathbf{U} + \frac{|\mathbf{k}_h|^2}{2\hat{\omega}K^2} \left[\partial_r N^2 - \frac{N^2 - f^2}{K^2} \partial_r \Gamma^2 \right] \right) + \frac{k_\lambda}{r} c_{g\lambda} + \frac{k_\phi}{r} c_{g\phi}. \quad (6)$$

Note that the metric terms ensure the propagation on great circles in the case of a uniform atmosphere at rest, as laid out in detail by Hasha et al. (2008)¹. Note that the representation in spherical coordinates comes with the drawback of a pole problem in the above relations when propagating very close to the pole. Practically, singularities due to division by zero, however, do not pose a serious problem as they only occur in close vicinity of the poles. To avoid potential problems, we do not consider wave generation where $|\phi| > 85^\circ$ (see Sec. 3c).

Finally, for the locally monochromatic field, its amplitude is governed by the wave-action equation

$$0 = \partial_t \mathcal{A} + \nabla_r \cdot (\mathbf{c}_g \mathcal{A}) + S, \quad (7)$$

¹Revisiting past studies we recognize that Ribstein et al. (2015) and Ribstein and Achatz (2016) omit some of the important metric terms so that their results should be interpreted with care.

for the wave-action density \mathcal{A} in physical space, where S denotes sources and sinks of wave action, such as the^{GSV} wave saturation as described below. Wave-wave interactions between IGWs as well as interactions between IGWs and the (subgrid-scale) geostrophic modes (GM) are neglected, and thus the wave action conservation is valid for any overlapping wave fields, provided their amplitudes are sufficiently weak. Numerous processes, e.g. wave refraction, can lead to rays crossing in physical space at so-called caustics, so that the assumption of local monochromaticity can break down in the course of the integration of the eikonal equations above. To avoid numerical instabilities due to this issue, we introduce the spectral wave-action density $\mathcal{N} = \mathcal{N}(\mathbf{r}, \mathbf{k}, t) = \sum_j \mathcal{A}_j(\mathbf{r}, t) \delta[\mathbf{k} - \mathbf{k}_j(\mathbf{r}, t)]$ in phase space, (c.f. Muraschko et al. 2015; Achatz 2022, and references therein) where the index j indicates any member of a possibly infinitely large and infinitely dense set of locally monochromatic fields that are being superposed. The resulting phase-space wave-action conservation then reads

$$\begin{aligned} 0 &= \partial_t \mathcal{N} + \nabla_{\mathbf{r}} \cdot (\mathbf{c}_g \mathcal{N}) + \nabla_{\mathbf{k}} \cdot (\dot{\mathbf{k}} \mathcal{N}) + \mathcal{S} \\ &= (\partial_t + \mathbf{c}_g \cdot \nabla_{\mathbf{r}} + \dot{\mathbf{k}} \cdot \nabla_{\mathbf{k}}) \mathcal{N} + \mathcal{S}. \end{aligned} \quad (8)$$

Note that due to the non-divergence of the six-dimensional phase-space velocity,

$$0 = \nabla_{\mathbf{r}} \cdot \mathbf{c}_g + \nabla_{\mathbf{k}} \cdot \dot{\mathbf{k}}, \quad (9)$$

the flux and the transport formulations in Eq. (8) are equivalent. Again, \mathcal{S} denotes both sources and the^{GSV} dissipation of phase-space wave action. Thus, the phase-space wave-action density, \mathcal{N} , is conserved along wave propagation paths up to the wave dissipation and generation^{GSV}. Moreover, the non-divergence (Eq. 9) of the phase-space velocity also implies that any phase-space volume following its rays conserves its volume content. As a consequence, rays cannot cross in phase space and caustics do not occur.^{GSV} Summarizing, Eqs. (3) to (6) and Eq. (8) form the basis for the forward ray-tracing of gravity waves.

b. Wave impact on the mean flow

To account for the impact of the wave perturbations on the mean flow, we note that the IGW-perturbation fluxes enter the mean flow tendencies as

$$\partial_t \mathbf{U}|_{IGW} = -\frac{1}{\bar{\rho}} \nabla \cdot (\bar{\rho} \langle \mathbf{v}' \mathbf{u}' \rangle) + \frac{f}{g} \mathbf{e}_r \times \langle \mathbf{u}' b' \rangle, \quad (10)$$

$$\partial_t \theta|_{IGW} = -\nabla \cdot \langle \mathbf{u}' \theta' \rangle, \quad (11)$$

where \mathbf{e}_r is the radial unit vector, g is Earth's gravity, and $\bar{\rho}$ and $\bar{\theta}$ are the reference density and potential temperature (Achatz et al. 2017, 2023). Moreover, \mathbf{v}' , b' , and θ' denote the IGW velocity, buoyancy, and potential-temperature perturbations, and \mathbf{u}' the horizontal component of \mathbf{v}' . The brackets, $\langle \cdot \rangle$, represent the phase average of the wave perturbations. Using the dispersion and polarization relations, they may be expressed as

$$\bar{\rho} \langle \mathbf{v}' \mathbf{u}' \rangle = \int \left[\frac{\hat{\omega}^2 \hat{\mathbf{c}}_g \mathbf{k}_h \mathcal{N} + f^2 (\mathbf{e}_r \times \hat{\mathbf{c}}_g) (\mathbf{e}_r \times \mathbf{k}_h \mathcal{N})}{\hat{\omega}^2 - f^2} \right] d^3 k, \quad (12)$$

$$\langle \mathbf{u}' \theta' \rangle = \int \left[\frac{\bar{\theta}}{g \bar{\rho}} \hat{\mathbf{c}}_{gr} \frac{f \mathcal{N}^2}{\hat{\omega}^2 - f^2} \mathbf{e}_r \times \mathbf{k}_h \mathcal{N} \right] d^3 k, \quad (13)$$

$$\frac{f}{g} \mathbf{e}_r \times \langle \mathbf{u}' b' \rangle = \frac{f}{\bar{\theta}} \mathbf{e}_r \times \langle \mathbf{u}' \theta' \rangle, \quad (14)$$

where we denote the horizontal wave vector as $\mathbf{k}_h = k_\lambda \mathbf{e}_\lambda + k_\phi \mathbf{e}_\phi$, and where $\hat{\mathbf{c}}_g = \mathbf{c}_g - \mathbf{U}$ is the intrinsic group velocity. Note that the elastic term, $\frac{f}{g} \mathbf{e}_r \times \langle \mathbf{u}' b' \rangle$, and the potential-temperature flux divergence, $\nabla \cdot \langle \mathbf{u}' \theta' \rangle$, are negligible where the Coriolis frequency, f , is small with respect to the intrinsic wave frequency, $|f| \ll |\hat{\omega}|$. Thus, the two terms^{GSV} are weak for non-hydrostatic waves in the mid to high frequency range^{GSV}. In addition, the momentum flux divergence may then be approximated with the pseudo^{GSV} momentum flux divergence, $\nabla \cdot (\bar{\rho} \langle \mathbf{v}' \mathbf{u}' \rangle) \approx \nabla \cdot \int \hat{\mathbf{c}}_g \mathbf{k}_h \mathcal{N} d^3 k$. Interestingly, the corresponding^{GSV} flux, often termed Eliassen-Palm flux, also determines the evolution of the mean-flow potential vorticity and the geostrophically and hydrostatically balanced mean flow even without any spectral restriction. It is thus often used in IGW parameterizations (e.g. Warner and McIntyre 2001; Orr et al. 2010; Bölöni et al. 2021). For a brief comparison of the two

approaches, see Appendix A. Recently, Wei et al. (2019) showed that the direct flux formulation more accurately represents the impact of an internal wave packet on the mean flow. Hence, we use the full set of fluxes shown in Eqs. (10) to (14).^{GSV}

Combined with the eikonal equations (Eqs. 4 to 6), wave propagation (Eq. 3), and wave-action conservation (Eq. 8), these relations form a closed prognostic system for transient wave propagation. Note that the equations are energy-conserving wherever both wave sources and dissipation are zero (not shown explicitly).

3. Gravity wave ray tracing

As pointed out in section 2, the subgrid-scale gravity wave dynamics are natively described on the rays of the corresponding gravity wave propagation. To include both the transience and the horizontal wave propagation, one may employ various techniques to obtain a numerical solution. Ray tracing has gained significant attention recently as an efficient and accurate method for simulating wave fields (Marks and Eckermann 1995; Muraschko et al. 2015; Amemiya and Sato 2016; Voelker et al. 2020; Bölöni et al. 2021). Here, we build on the implementations of Bölöni et al. (2021) and Kim et al. (2021) and extend the approach by the horizontal wave propagation and the full flux calculation (Eqs. 10 to 11). While we present a broad overview in this section, we would like to refer the reader to Appendix A for additional details.

a. Representation of rays as phase-space ray volumes

One of the major challenges for ray tracing is the problem of caustics and the subsequent ambiguity of the notion of wave amplitudes and wave energy of a local spectrum. As laid out above, it is possible to reformulate the wave action conservation as a transport equation in the 6-dimensional phase space. The non-divergence of the phase-space velocity (Eq. 9) implies that any phase-space volume following its rays conserves its volume content, i.e.

$$\begin{aligned}
 0 &= d_t (dx dy dz dk_x dk_y dk_z) \\
 &= d_t \left(r^2 \cos \phi d\lambda d\phi dr dk_\lambda dk_\phi dk_r \right).
 \end{aligned} \tag{15}$$

where (x, y, z) are the Cartesian coordinates, and (k_x, k_y, k_z) are the wave-vector components in these coordinates. In Cartesian coordinates one has even

$$0 = \partial_x c_{gx} + \partial_{k_x} \dot{k}_x \quad (16)$$

$$0 = \partial_y c_{gy} + \partial_{k_y} \dot{k}_y \quad (17)$$

$$0 = \partial_z c_{gz} + \partial_{k_z} \dot{k}_z \quad (18)$$

so that

$$0 = d_t(dxdk_x) = d_t(dydk_y) = d_t(dzdk_z). \quad (19)$$

Such a simple splitting relies on the independence of the spatial coordinates and^{GSV} does not exist in spherical coordinates. The approach taken in MS-GWaM, for the time being, is to divide the phase-space content with non-zero wave-action density, \mathcal{N} , into finite-size small ray volumes, with extent $\Delta(\lambda, \phi, r, k_\lambda, k_\phi, k_r)$. Within the spanned ray volume, the wave action density, N , is assumed constant. The ray volume content is then propagated according to Eqs. (3) to (6) following a central carrier ray. The change in physical extent, $\Delta(\lambda, \phi, r)$, is determined using rays at the faces of the ray volumes carrying identical wave properties (k_λ, k_ϕ, k_r) as in the central carrier ray but being exposed to deviations in the background fields. In particular, the ray-volume extent is approximated as locally Cartesian by

$$\Delta(x, y, z) = (r \cos \phi \Delta\lambda, r \Delta\phi, \Delta r), \quad (20)$$

$$\Delta(k_x, k_y, k_z) = \Delta(k_\lambda, k_\phi, k_r) \quad (21)$$

where the new $\Delta(k_x, k_y, k_z)$ is determined by Eq. (19), and then inverted using Eq. (21) to finally obtain the new $\Delta(k_\lambda, k_\phi, k_r)$. Note that this procedure, albeit converging for infinitesimally small ray volumes, implies the following simplification. In a uniform atmosphere at rest, where the group velocity differences between the opposing ray-volume faces are exactly zero, the ray-volume extent in spherical coordinates, $\Delta(\lambda, \phi, r)$, is exactly conserved. This implies, however, that any ray volume propagating polewards must shrink in the tangent-linear extent Δx and expand in spectral width Δk_λ (and vice versa for southward propagation). Although this effect may be small in

regions sufficiently separated from the pole, we plan to apply an advanced method to remove this potential^{GSV} problem to the next version of MS-GWaM.

b. Coupling of Lagrangian particles to the Eulerian mean flow

The coupling between the large-scale flow and the wave perturbations necessitates linking the Lagrangian wave representation to the Eulerian model grid. For the evaluation of the modulation equations, we linearly interpolate all necessary mean fields and their gradients to the ray-volume center or faces using a first-order Taylor expansion. In particular, the group velocities are calculated at the physical boundaries of the ray volume (see App. B1). This serves a dual purpose: the mean of the group velocities on opposing ray-volume faces may be used to advance the location of the central carrier ray, and the difference between them serves as an estimate for the compression or inflation of the ray volume in physical space. The phase-space extent is then determined as described above.

To account for the impact of waves on the mean flow, it is necessary to differentiate between the vertical and horizontal components, considering possibly irregular horizontal grid structures. The vertical gradient of the wave flux, i.e., $\partial_r(\bar{\rho}\langle w'u'\rangle)$ in Eq. (10), is computed following Muraschko et al. (2015), Bölöni et al. (2016, 2021). In particular, the vertical flux associated with a grid cell boundary is integrated over all ray volumes contained in the vertically staggered cell that covers the desired cell boundary (for more details, see Fig. 1a in Bölöni et al. 2021). The gradients are then computed from the centered difference of the vertical cell-boundary values. For the horizontal fluxes, the grid-cell averaged values (rather than those at the boundaries) are calculated to avoid problems with complex grid geometries. We integrate all ray volumes whose carrier rays are contained in the chosen grid cell's volume. To mend errors due to ray volumes overlapping multiple adjacent cells, the obtained flux fields are horizontally smoothed (App. B4). The resulting fields and their divergences (Eqs. 10 and 11) then contribute to the tendencies provided by the parametrization.

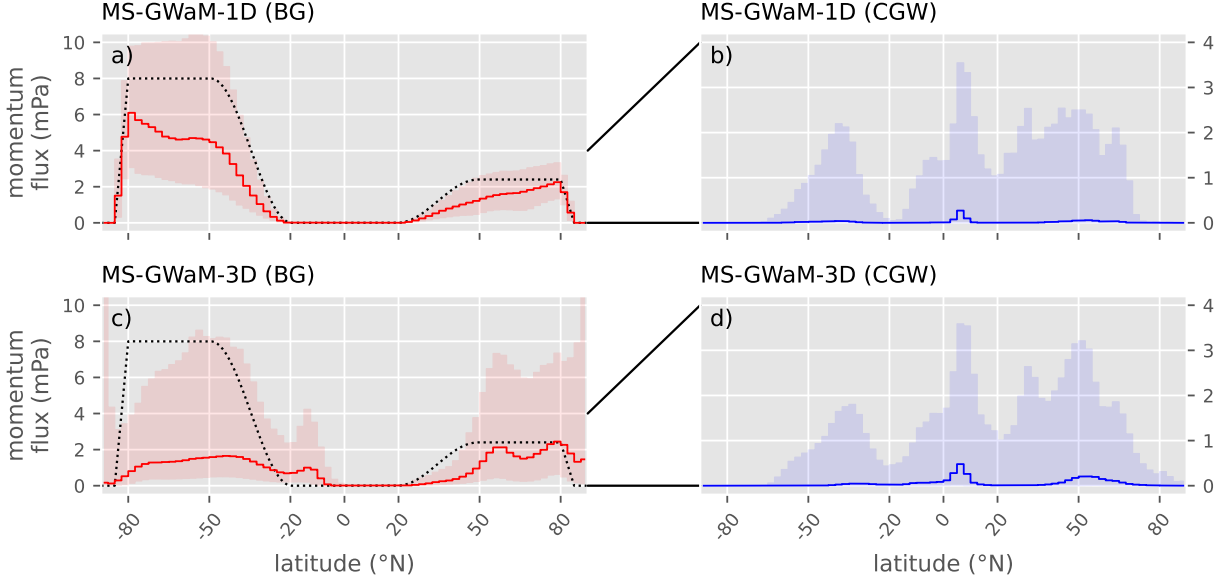


FIG. 1. Zonally averaged absolute vertical fluxes of horizontal momentum at 16 km height for MS-GWaM-1D (a-b) and MS-GWaM-3D (c-d) for June 1991. The solid lines represent the 50th percentile (median), the surfaces show the ranges from the 10th to the 90th percentiles. Results are separated into background waves (a, c) and convectively generated waves (b, d). The black dotted lines represent the launched absolute momentum fluxes at 300 hPa during the summer solstice.

c. Sources and sinks of internal gravity waves

Similar to Bölöni et al. (2021) and Kim et al. (2021), the present implementation of MS-GWaM utilizes two sources of gravity waves as a lower boundary condition (Fig. 1). In particular, a background source in the middle to high latitudes, accounting, e.g. for IGWs emitted from jets and fronts, as well as a convective source, are employed. The former prescribes at a given launch level a seasonally varying pseudo-momentum flux with a spectral shape following the Desaubie spectrum (c.f. Orr et al. 2010). At the solstice, it has a latitudinal profile with winter hemispheric fluxes of $F_w = 8 \text{ mPa}$, no fluxes for latitudes $\phi \in [20^\circ\text{S}, 20^\circ\text{N}]$, and summer hemispheric fluxes of $F_s = 2.4 \text{ mPa}$. No background waves are launched at latitudes higher than $|\phi| > 85^\circ$. The different regimes are connected through smooth transitions. The profile oscillates in time with a sinusoidal yearly cycle. Summarizing, we employ a latitudinal profile, $\alpha(\varphi)$, and a total absolute momentum

flux at the lower boundary during the Northern summer solstice, F_{sol} ,

$$\alpha(\varphi) = \begin{cases} \min\left(1, \max\left(0, 1 - \frac{\varphi-80}{5}\right)\right) & \text{if } \varphi \geq 80 \\ 1, & \text{if } \varphi \in [50, 80) \\ \frac{1}{2}\left(1 - \cos\left(\pi\frac{\varphi-20}{30}\right)\right) & \text{if } \varphi \in [20, 50) \\ 0 & \text{else} \end{cases}, \quad (22)$$

$$F_{sol}(\varphi) = \alpha(\varphi)F_s + \alpha(-\varphi)F_w, \quad (23)$$

where φ is the latitude in units $^\circ\text{N}$. The absolute momentum flux at the lower boundary condition then reads

$$F_{am} = \frac{1}{2} \left[F_{sol}(\varphi)(1 + \cos \tau) + F_{sol}(-\varphi)(1 - \cos \tau) \right], \quad (24)$$

with the non-dimensional time difference, $\tau = 2\pi(t - t_{sol})/1 \text{ y}$, relative to the time of the Northern summer solstice, t_{sol} . These background waves are launched at every time step^{G_{SV}} at a height corresponding to a pressure of 300 hPa (black, dotted line in Fig. 1a and c) with a momentum flux which is equally divided into 4 horizontal directions as done by Bölöni et al. (2021). In particular, we construct a ghost layer at the launch altitude within which ray volumes are allowed to propagate vertically only. At every launch interval, that is every 60 s (equivalent to the model time step), the fraction of the ray volume which has propagated out of the ghost layer, is separated and activated. Only then it will propagate freely according to the modulation equations. Ray volumes which are reflected within the ghost layer are discarded. More technical information on the launch process can be found in the work of Bölöni et al. (2021). This background^{G_{SV}} wave energy source is directionally homogeneous, with a purely latitudinal profile on the 300 hPa pressure surface. Additionally, convectively generated waves are considered with a launch spectrum^{G_{SV}} as described by Kim et al. (2021). In their formulation, the areal fraction of the convective latent heat release, ϵ_q , inversely controls the total entropy forcing and thus the launch momentum flux (Kim et al. 2021). Here, we increase the area fraction to $\epsilon_q = 7\%$, resulting in a reduced gravity wave flux.

For the convective source we couple MS-GWaM to the convection parameterization and utilize the convection strength and depth calculated within. The ray volumes are then launched at the cloud top and under consideration of the background wind.^{GSV} As an example of the resulting lower boundary conditions, we show the absolute vertical momentum fluxes, defined by

$$F_{am} = \bar{\rho} \left(\langle w'u' \rangle^2 + \langle w'v' \rangle^2 \right)^{\frac{1}{2}}, \quad (25)$$

through the surface at a constant height of 16 km for June 1991 (Fig. 1). The thick line presents the median of the zonally averaged fluxes during the month, and the shading around the median shows the range between the 10th and 90th percentiles, highlighting the variability in the fluxes. Even though this height is rather close to the launch altitudes, we observe that the horizontal wave propagation changes the statistics of the vertical fluxes of background waves (Fig. 1a and c). In particular, we note that the gravity wave transience leads to a reduction of the median absolute momentum fluxes and a strong variability with fluxes regularly exceeding the launch flux. This can be explained by a spatially and temporally varying mean flow through which the waves propagate from the launch level to the depicted 16 km altitude. For instance, the waves may encounter reductions and increases of their vertical group velocity, critical layers, or vertical reflection. In addition, the horizontal propagation leads to both an increased dissipation below 16 km as well as a horizontal redistribution, effectively changing the wave flux statistics. Comparing Fig. 1a and b we thus find a reduced median flux for MS-GWaM-3D and background waves far outside the mid to high latitude generation regions.^{GSV} In contrast to the background source^{GSV}, the convectively generated waves show rather similar statistics at this altitude between MS-GWaM-3D and 1D (Fig. 1b and d). Naturally, their statistics differs from the background waves as convective events are spatially and temporally rather sparse but can lead to high momentum fluxes. Thus, the spatio-temporal median is very low, while the peak momentum fluxes are comparable to the background waves.^{GSV}

Finally, we would like to add that the launch fluxes, F_w and F_s , as well as the area fraction, ϵ_q , were tuned to achieve a realistic zonal mean mesopause. In particular, both the wind reversal and the summer hemispheric cold pole are expected to occur at approximately 80 km (see discussion of mean model states in Sec. 4a). To avoid high computational costs due to optimization algorithms,

short runs were considered, integrating the model for 2 weeks in both seasons. The model results, calculated for a physical range of the three tunable parameters, were then compared and the best fit was chosen. The resulting directional momentum fluxes compare in order of magnitude with satellite observations at altitudes 30 to 40 km but differ in horizontal distribution (Jiang et al. 2006; Ern et al. 2018; Hindley et al. 2020; Polichtchouk et al. 2022, direct comparisons not shown). The latter is, however, expected given MS-GWaM incorporates a flow-independent background source.^{GSV}

The two sources of wave energy are accompanied by a saturation parametrization following Bölöni et al. (2016, 2021) which is based on the idea of Lindzen (1981) but in a spectrally integrated manner. In particular, the threshold for static instability is formulated for the wave action as follows,

$$\int_{\mathbb{R}^3} \frac{k_r^2 |\mathbf{k}_h|^2}{\hat{\omega} K^2} \mathcal{N} d^3 k = \mathcal{P} < \frac{\bar{\rho}}{2}. \quad (26)$$

Note, that for a quasi-monochromatic wave, this relation reduces to the well-known threshold, $|B_w|^2 < N^4/k_r^2$, with B_w being the amplitude of IGW buoyancy. The concept of the integrated density perturbation, \mathcal{P} , is then used in a discrete sense and rewritten as the sum over all physically overlapping ray volumes, j , at the location, \mathbf{r}_b , such that

$$\mathcal{P} = \sum_j \mathcal{P}_j = \sum_j \frac{k_{rj}^2 |\mathbf{k}_{hj}|^2}{\hat{\omega}_j K_j^2} \mathcal{A}_j \alpha_j. \quad (27)$$

Here, $\mathcal{A}_j = \mathcal{N}_j \Delta k_\lambda \Delta k_\phi \Delta k_r$ and α_j are the ray volume's total wave action and the spatial fraction that the j th ray volume takes of the volume of the cell it is contained in, respectively.^{GSV} Thus, rather than each individual spectral component, we consider a spectrally integrated saturation. The reduction of the individual wave action components, \mathcal{A}_j , to their saturation value, \mathcal{A}_j^* , is then achieved through setting

$$\mathcal{N}_j \rightarrow \mathcal{N}_j^* = \mathcal{N}_j \left[1 - 2\kappa K_j^2 \Delta t \right], \quad (28)$$

with the turbulent diffusivity coefficient

$$\kappa = \max\left(0, \frac{\mathcal{P} - \frac{\bar{\rho}}{2}}{2\Delta t \sum_j \mathcal{P}_j K_j^2}\right). \quad (29)$$

Saturation is thus triggered where the instability threshold (Eq. 26) is violated by the constructive interference of locally overlapping internal waves. All wave amplitudes, or equivalently wave action densities, are then set to the corresponding saturation values. Note that Eq. (29) does not imply that the turbulent diffusivity diverges as $\Delta t \rightarrow \infty$. Because at the beginning of each time step $\mathcal{P} \leq \frac{\bar{\rho}}{2}$, the numerator of the ratio is at best growing linearly with Δt , so that κ always ends up finite. This spectral saturation implementation was shown to compare well to wave-resolving simulations in idealized cases by Bölöni et al. (2016). Furthermore, it is planned to couple the saturation scheme to the turbulence parameterization of the underlying atmospheric model, ICON. An in-depth analysis of the breaking processes and the impact of the spectral saturation on a global scale is hence left to a future study.^{GSV}

4. Atmospheric simulations with UA-ICON and MS-GWaM-3D

Building on Bölöni et al. (2021) and Kim et al. (2021), who introduced MS-GWaM-1D, we choose to work with the ICON model with its upper-atmosphere extension (Zängl et al. 2015; Borchert et al. 2019). Here, we use version *2.6.5-nwp1b*^{GSV} with a horizontal resolution of approximately 160 km (model grid R2B04) and the physics packages for the numerical weather prediction (NWP) and the upper atmosphere. Note, that MS-GWaM replaces the non-orographic gravity wave drag but leaves the operational orographic wave parameterization intact (in particular, Lott and Miller 1997). Through the coupling to the mean wind, the latter thus indirectly interacts with MS-GWaM.^{GSV} The setup has a model top of 150 km with vertical grid extent of a few tens of meters in the boundary layer, 700 to 1500 m in the stratosphere, and a maximum of approximately 4 km in the lower thermosphere. A sponge layer acts above an altitude of 110 km which is why we restrict our analysis to altitudes below 100 km. The model is initialized with IFS analysis data below 60 km and with the climatological thermodynamic state at rest above. It is then spun up for a month to exclude adjustment effects in our analysis. These runs are repeated to simulate June and December for the

years 1991 through 1998. Additionally, we deploy runs for June and December 1991 with extended diagnostics. In particular, the free parameters controlling the launch fluxes are the convective area fraction for the convectively generated waves and the summer and winter launch amplitudes of the background waves (see Sec. 3c). In general, stronger gravity-wave launch fluxes shift the wave saturation to lower altitudes, leading to a lower wind reversal at the mesopause. Comparisons of simulations with the horizontal wind model HWM (hereafter HWM2014, Drob et al. 2015) and the empirical temperature model NRLMSIS2.1 (hereafter MSIS, Emmert et al. 2022) then give a good estimate for the performance of the chosen parameters. The HWM2014 and MSIS are chosen based on their wealth of incorporated data in the middle and upper atmosphere in the time range of our simulations. In particular, they incorporate reanalysis, ground based datasets, and satellite based observations (for more detail see Drob et al. 2015; Emmert et al. 2021, 2022). The reference climatologies are then generated for exactly the simulated months.^{GSV} With the help of short simulations spanning a large parameter space, we identified an optimum with an area fraction of $\varepsilon_q = 7\%$, a winter launch flux of $F_w = 8 \text{ mPa}$, and a summer launch flux of $F_s = 2.4 \text{ mPa}$ (for more detail, see Sec. 3c).

a. Zonal mean flow

To test the general performance of the gravity wave parametrization, we analyze the zonal-mean zonal wind and temperatures as composites over 8 simulations of June and December (Fig. 2 and 3). To highlight the general effect of the parameterizations and visualize the general model performance, we accompany the data from simulations without non-orographic gravity wave parameterization. Naturally, the runs including a gravity wave drag parametrization mend model biases and thus differ significantly from the runs without. The comparison is, therefore, to be understood as a reference for the general behavior of ICON in the present setup and in how far model biases stem from the lack of a gravity wave drag parametrization or may be rooted elsewhere. Additionally, we show the reference climatologies HWM2014 and MSIS. Note that, as described above, both versions of MS-GWaM were tuned such that the mesopause height at $z \approx 80 \text{ km}$ agrees with the HWM2014. In general, MS-GWaM-1D and 3D produce physical zonal-mean zonal winds with the expected wind reversals in both the summer and winter hemispheres (Fig. 2b-d, f-h). As one may expect, runs

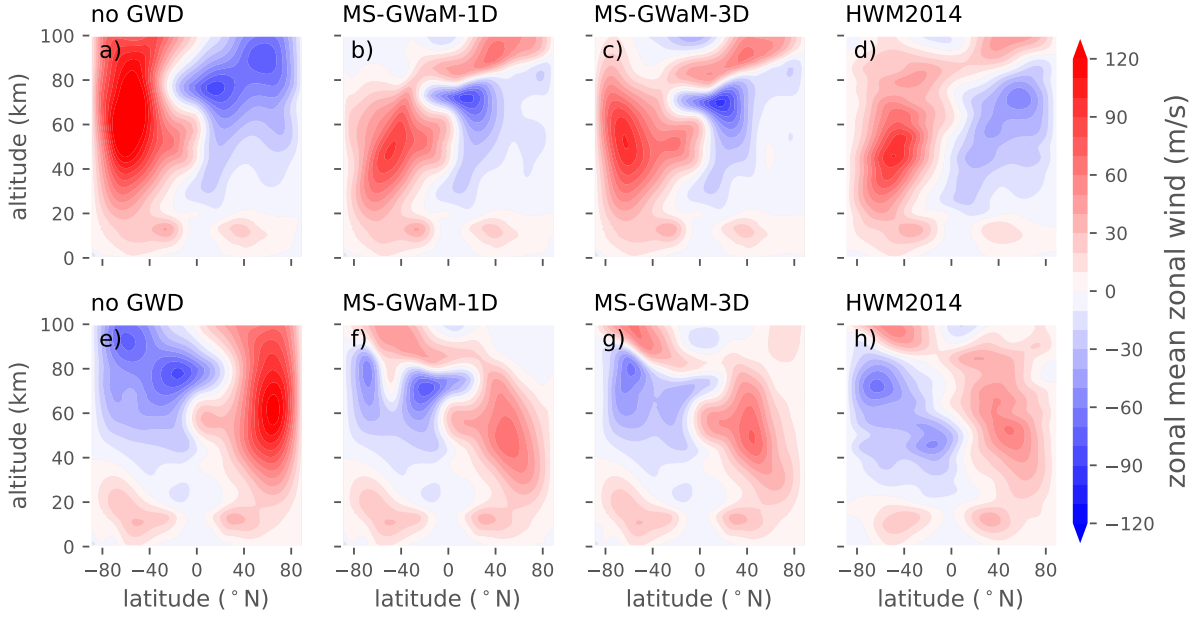


FIG. 2. Zonal mean zonal winds from composites of runs for June (a-d) and December (e-h). The composites correspond to averages for the years 1991 through 1998. Runs from MS-GWaM-1D (b, f) and MS-GWaM-3D (c, g) are compared to simulations without any non-orographic IGW parameterization (a, e) and the HWM2014 climatologic model (d, h).

with the same model setup but without any non-orographic parameterization are subject to strong jets and entirely lack the mesopause reversal (Fig. 2a and e).

Notable differences to the HWM2014 can be seen in the summer hemispheric jets, in the tropical stratosphere, and in the Antarctic winter jet. Comparing the two MS-GWaM results with the run without any non-orographic gravity wave drag parameterization (Fig. 2a and e) we find that the tropical stratospheric jet at $z \approx 50$ km height is a^{GSV} robust feature of the current model version, which is^{GSV} present in all three runs. The aforementioned tuning runs indicated that there is little to no influence on the structure by the tuning parameters^{GSV} (not shown). We thus conclude that it is^{GSV} generally independent of the gravity wave parameterization. The weak northern summer jet, however, seems to be related to the transient parameterization in general, as it is present in runs with both MS-GWaM-1D and MS-GWaM-3D (Fig. 2b and c). While we note a similar bias in the work of Bölöni et al. (2021), the runs without any non-orographic gravity wave parameterization do not suffer from this bias (Fig. 2d).^{GSV} Finally, we observe that the slant of the Antarctic winter jet towards the equator is not entirely reproduced by MS-GWaM-3D (Fig. 2c). This is due to

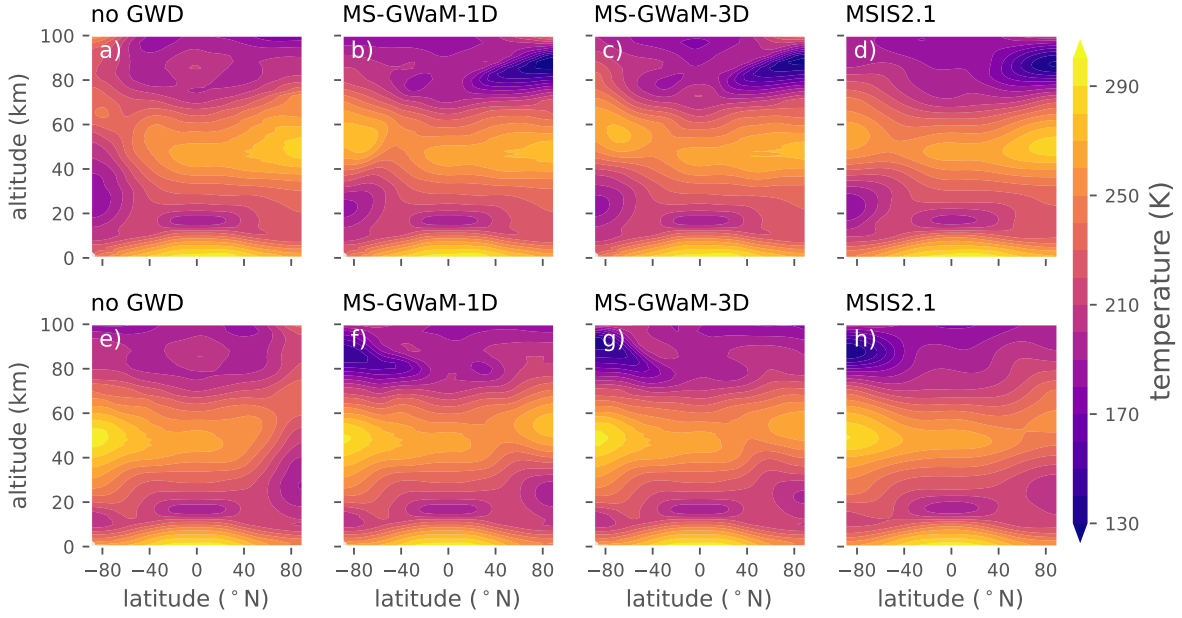


FIG. 3. Like Fig. 2 but for zonally averaged temperatures. For comparison, we show the climatological model MSIS2.1 (d, h).

a modified zonal and meridional gravity wave drag in the Southern hemisphere^{GSV} above 60 km altitude in MS-GWaM-3D as opposed to MS-GWaM-1D as will be discussed in Sec. 4c^{GSV}. Possible reasons for the modified^{GSV} wave drag might be improper spectral characteristics of the current background source, errors near the pole due to the representation of the ray-volume extent in spherical coordinate systems (c.f. Sec. 3a), or even co-dependencies of the columnar gravity wave parameterization with other parameterizations such as the employed orographic wave drag parameterization. Moreover, other components of the model, such as the^{GSV} radiation scheme or the modified ozone climatology, are tuned to produce realistic temperature distributions in combination with the standard orographic wave drag.^{GSV} In general, the confidence in the present implementation is high, as MS-GWaM-1D was validated by Bölöni et al. (2021); Kim et al. (2021) and MS-GWaM-3D was validated against the results of Wei et al. (2019) using an idealized cubic geometry implemented in ICON (not shown). However, a more detailed analysis may be needed to identify the reasons behind the phenomenon and mend the setup accordingly.

Similar to the zonally averaged zonal winds, we find that the zonally averaged temperatures and the corresponding MSIS fields agree well (Fig. 3). In particular, the MS-GWaM reproduces the cold summer pole at the mesopause as well as the warm winter pole associated with the stratopause

(Fig. 3b-c and f-g). These features are naturally not present when the non-orographic gravity wave drag parameterization is switched off (Fig. 3a and e).

In general,^{GSV} the zonal-mean model state generally seems to be moderately^{GSV} affected by enabling a 3-dimensional wave propagation in MS-GWaM. While the runs with the transient parameterizations generally exert some bias in the northern summer hemisphere, the Antarctic winter jet is too strong at altitudes around 50 km to 80 km for MS-GWaM-3D. Runs for the month December do not contain these systematic biases.^{GSV} This resembles the findings of Bölöni et al. (2021) where a weak dependency of the zonal-mean wind on the transience of the gravity wave parameterization was detected. Albeit somewhat counter-intuitive, it may not be a surprise, as the spatial and temporal averages represent the quasi-steady state of the model setups. These in turn are tuned to approximate a similar zonal-mean model state. It was, however, also shown that both the transience and the localization of the gravity waves can have significant impacts on the structure of the horizontal mean flow (e.g. Sato et al. 2009; Sacha et al. 2016; Ehard et al. 2017). For instance, the mean-state results may change if a more realistic spatio-temporal distribution of the wave source spectrum was employed. While the investigation of realistic source distribution is left for future work, in the following sections we focus on the nature of 3-dimensional propagation of parameterized IGWs, examining wave action fluxes and budgets as well as horizontal structures of IGW momentum fluxes and mean wave drags.

b. Global 3-dimensional IGW distribution

Gravity waves are generally 3-dimensional phenomena that are present in large parts of the atmosphere. While wave-resolving simulations can provide^{GSV} insights into global wave activity, they typically span short model times due to the limitations of both computational resources and^{GSV} required storage. Additionally, the separation of IGWs from other dynamics and their characterization are generally non-trivial tasks. Being based on a multiscale WKB theory (Achatz et al. 2017), MS-GWaM simulates the global behavior of non-orographic gravity waves without the need to explicitly resolve their fast varying phases. As a result, it can be used to predict global distributions of phase-space wave action densities as well as derived quantities such as momentum fluxes and the resulting wave drag. As an example, we analyze the global wave action budget and augment it with the zonal wave drag to illustrate the resulting effect on the mean flow^{GSV}.

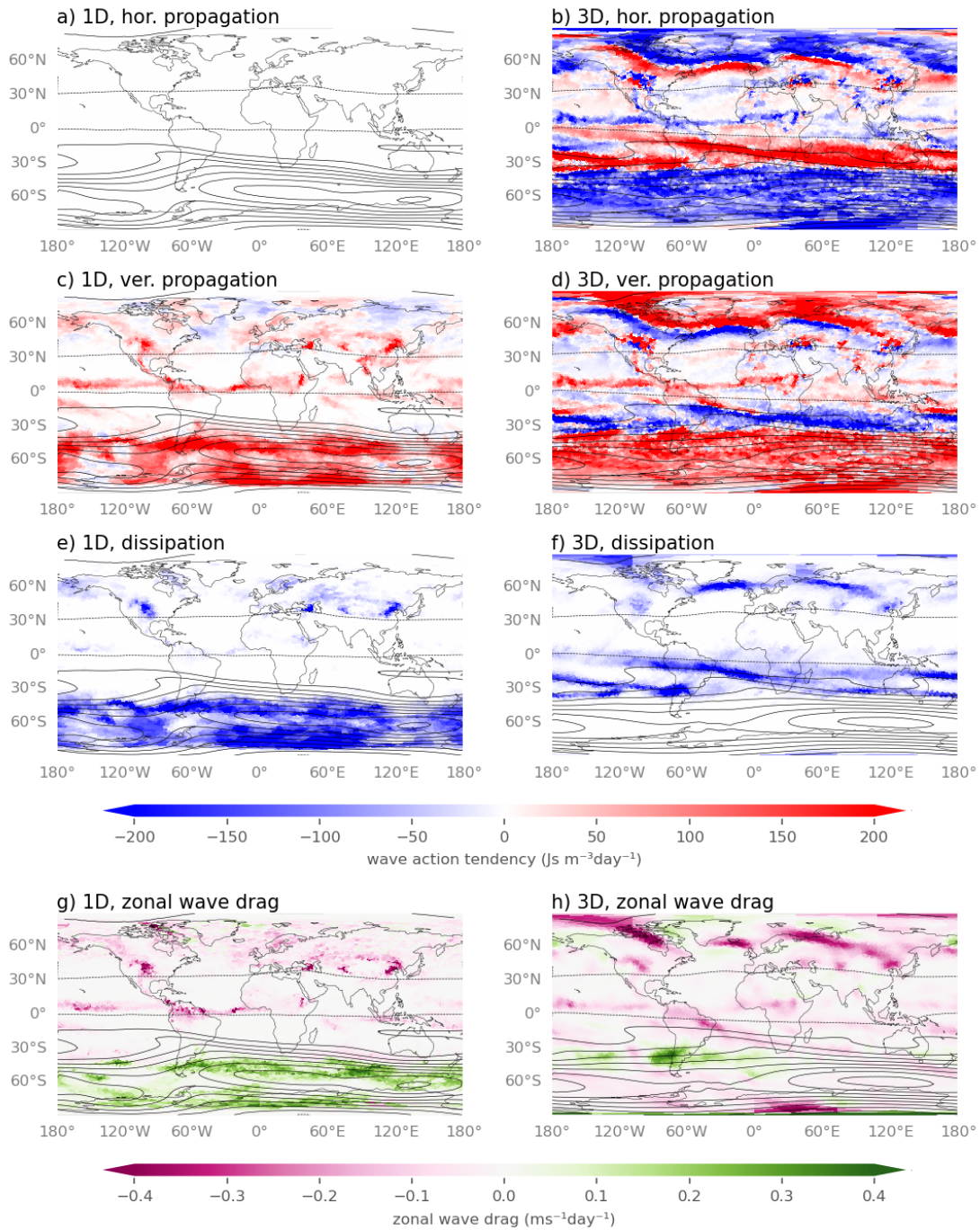


FIG. 4. Wave action tendencies for MS-GWaM-1D (left column) and MS-GWaM-3D (right column) due to horizontal wave propagation (a, b), vertical wave propagation (c, d) and wave dissipation (e, f). The last row depicts the corresponding zonal wave drag. All tendencies are 10-day averages for June 10-20 1991 at an altitude of $z \approx 25 \text{ km}^{\text{GSV}}$. Additionally, contours of the zonal wind in steps of $10 \text{ m s}^{-1 \text{GSV}}$ are shown.

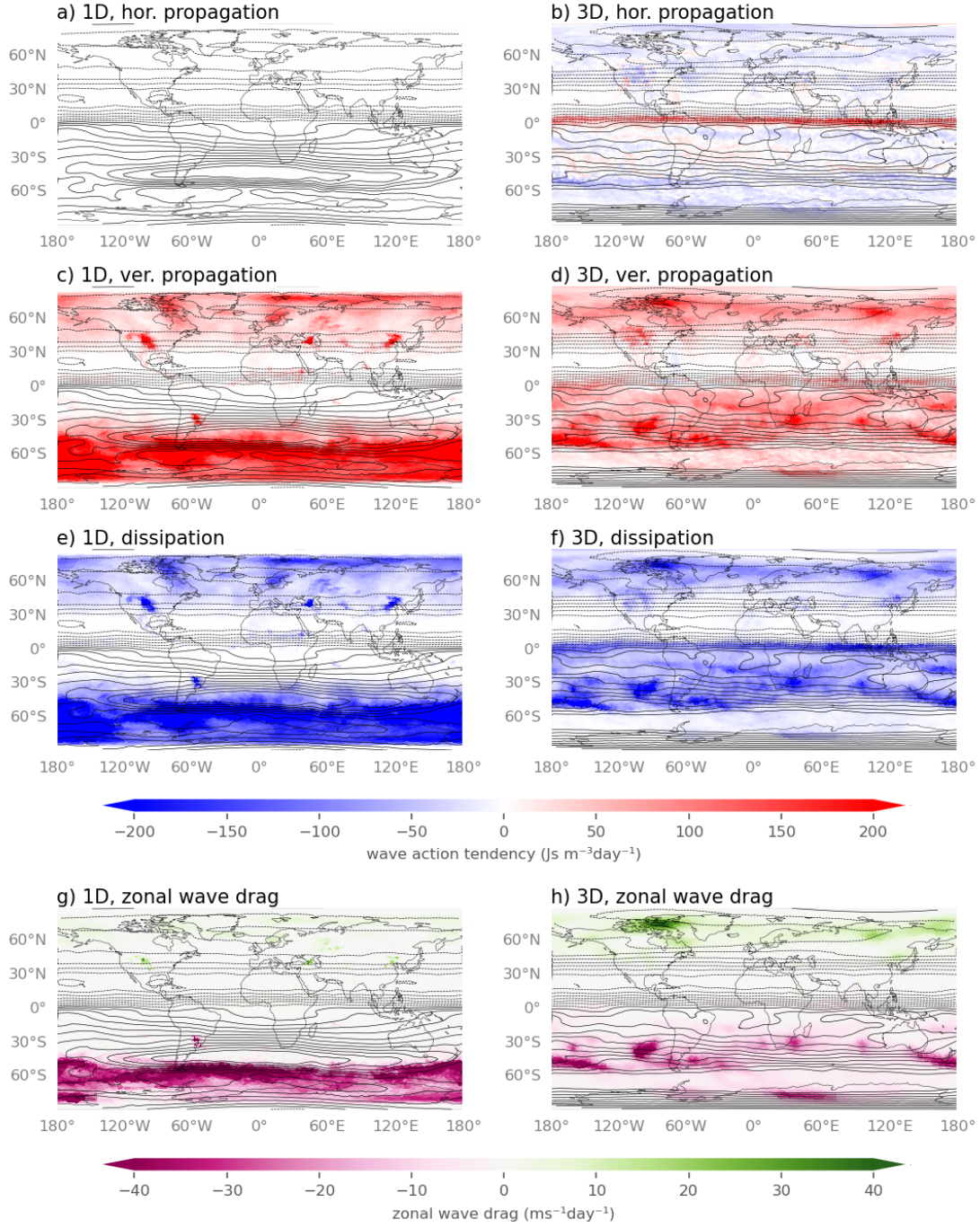


FIG. 5. As Fig. 4 but for $z \approx 60 \text{ km}^{\text{GSV}}$

Consider the phase-space integrated wave action conservation (Eq. 8), averaged in time,

$$-\frac{\Delta \mathcal{A}}{\Delta t} = \nabla_h \cdot \overline{c_{gh} \mathcal{A}} + \partial_r \overline{c_{gr} \mathcal{A}} + \overline{S}, \quad (30)$$

where we define $(c_{gh}, c_{gr})\mathcal{A} = \int (c_{gh}, c_{gr})\mathcal{N}d^3k$, and the overbars denote the temporal average over the time interval, Δt . Here, the three right-hand side terms correspond to the temporally averaged wave-action tendency contributions from the horizontal wave propagation, the vertical wave propagation, and the wave saturation. Moreover, the left-hand term is small for sufficiently long averaging intervals. For a sufficiently small left-hand-side of Eq. (30) while preserving the planetary wave structure, we choose $\Delta t = 10\text{d}$ and show the predictions of the right-hand side contributions by MS-GWaM-1D and MS-GWaM^{G_{SV}}-3D at altitudes of approximately 25 km and 60 km for June 10-20, 1991. While the 25 km level shows the stark differences between the 1D and 3D schemes, the wave dynamics at 60 km altitude highlight the interaction with the Antarctic polar night jet in more detail.^{G_{SV}}

As one may expect, MS-GWaM-1D predicts a balance between the vertical wave action^{G_{SV}} propagation and dissipation at either altitude^{G_{SV}} (Figs. 4 and 5, panels c and e). Thus, wave breaking and strong mean-flow impacts^{G_{SV}} can only occur where IGWs were previously able to vertically propagate through the wind shear of the underlying air column. Negative values for the change of wave action due to vertical propagation are associated with a finite temporal averaging interval, Δt . For instance, propagating mean-flow structures such as planetary waves may lead to changes in the wave action budget which adjust only on the time scale of the wave propagation. Although not linearly related, the strongest zonal wave drags occur where the wave dissipation is high. At the rather low altitude of 25 km this results in a rather uniform distribution of wave dissipation and drag in the Southern hemisphere, accompanied with intermittent convective events in the Northern hemisphere (Fig. 4e to g)^{G_{SV}}. Running the same case with MS-GWaM-3D, we find that both the contributions due to the horizontal and vertical propagation are of similar magnitude at an altitude of 25 km^{G_{SV}}, such that the resulting balance includes all terms (Fig. 4b, d, and f). Near horizontally sheared wind structures, such as the edges of the Antarctic winter jet, the two contributions from the horizontal and vertical propagation form inverted dipoles associated with wave refraction phenomena. In the case of the mentioned Antarctic winter jet, as we will show below, this corresponds to the often observed wave refraction into the jet (e.g. Ehard et al. 2017; Hindley et al. 2020). Interestingly, the wave refraction follows the structure of the resolved planetary waves and ultimately leads to a shift of lower-level wave action^{G_{SV}} dissipation towards regions of strong horizontal shear, as for instance found between the summer and winter jets (Fig. 4f). Despite

the different launch amplitudes (see Sec. 3c) all contributions have similar magnitudes on both hemispheres. Correspondingly, the horizontal propagation significantly modifies the zonal wave drag at 25 km. While the Southern hemispheric drag is much reduced, the Northern hemisphere exhibits comparatively strong drags near planetary wave structures. Interestingly, the wave action budgets change structurally with altitude. At $z \approx 60$ km, both the budgets of MS-GWaM-1D and MS-GWaM-3D are mostly controlled by vertical wave action propagation and dissipation (Fig. 5c to f). In contrast to the lower altitude, the horizontal wave action propagation is much reduced. However, the horizontal propagation through lower altitudes shifts the action dissipation and wave drag near the Southern winter jet towards the equator (Fig. 5e - h). We suspect this shift to cause the missing wave drag at higher altitudes near the pole, leading to a biased jet structure in the zonal mean. These results suggest an important influence of the horizontal propagation near the Antarctic winter jet and thus we analyze the the zonal mean drag structures in the following.^{GSV}

c. Wave propagation and drag^{GSV} in the vicinity of horizontally sheared jet structures

Expanding on the horizontal refraction behavior found in the horizontal maps (Figs. 4 and 5) we show zonal averages of wave action fluxes (Fig. 6) and the corresponding wave drag (Fig. 7) temporally averaged over free runs for Junes and Decembers 1991 through 1998^{GSV}. By construction, MS-GWaM-1D only allows for vertical propagation (Fig. 6a and c). The corresponding wave-action tendency is thus associated with the vertical wave-action flux convergence. The consequently generated wave drag accelerates the zonal wind structures, with maxima occurring at the mesopause (Fig. 7a and c). Note, that maximum wave action flux convergences are not equivalent to the maximum wave drag due to the scaling with the wave vector (compare Sec. 2).^{GSV} MS-GWaM-3D shows strong horizontal propagation in regions of strong horizontal and vertical shear, such as jet edges (Fig. 6b and d). Notably, in southern-hemispheric winter the wave action flux vector points northward near the South Pole, i.e. into the Southern winter jet, (Fig. 6b). Consequently, the polar wave-action fluxes are reduced at altitudes near the mesopause and the wave drag maximum is weaker south of 75°S ^{GSV} (Fig. 6b and Fig. 7b). Moreover, the equatorial regions are strongly affected by the horizontal wave propagation (Fig. 7b and d). Here, the wind shear is generally strong but the mean wave action fluxes are weak due to the intermittency of the

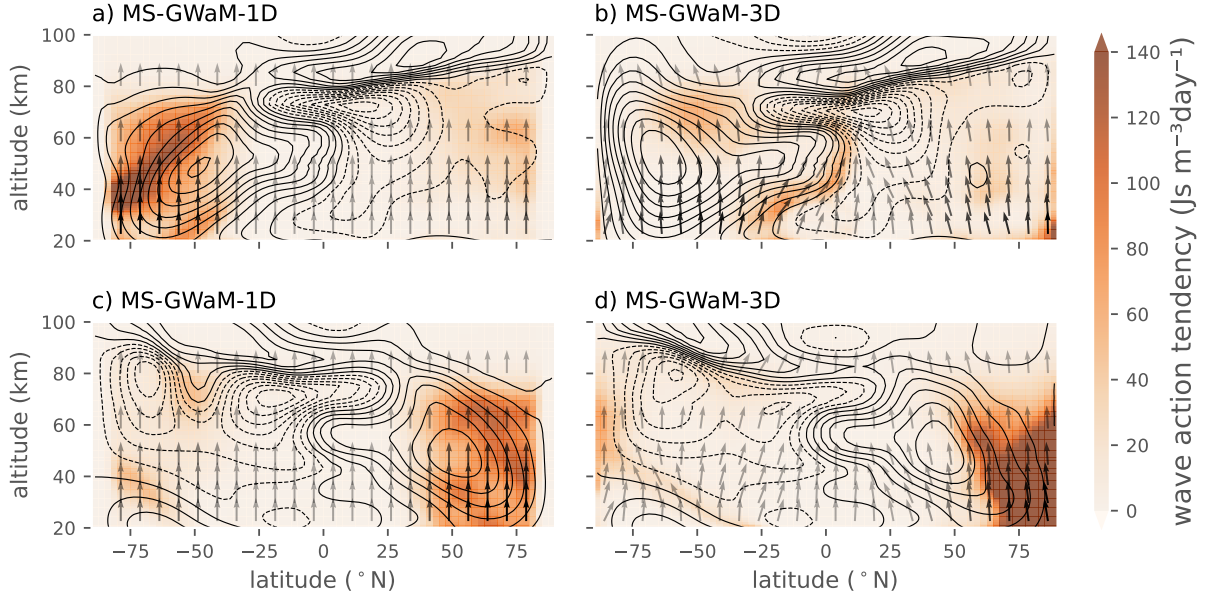


FIG. 6. Wave action changes due to wave propagation in MS-GWaM-1D (a, c) and MS-GWaM-3D (b, d) for composites of June (a-b) and December (c-d). The field is overlaid with vectors of wave action fluxes. They are scaled with respect to the plot dimensions and units, the horizontal direction is enhanced by a factor of 3 for visualization. The arrow transparency represents the wave action flux strength. The contours represent the corresponding zonally averaged zonal wind with 10 m s^{-1} increments, with dashed and solid lines for negatives and non-negatives, respectively. See Fig. 7 for the corresponding wave drag.

convective wave source.

GSV

To highlight the dynamics near the Antarctic winter jet, we additionally show the zonal and meridional wave drags for both MS-GWaM-1D and MS-GWaM-3D near the jet, averaged for all Junes (Fig. 8). Here, the reduced zonal wave drag for MS-GWaM-3D, south of 75°S becomes particularly visible (Fig. 8a - b). Moreover, the maximum zonal wave drag is shifted southward due to the horizontal propagation. Stronger differences can be seen for the generally weaker meridional component (Fig. 8c - d). In particular, it changes sign and exerts a southward drag on the jet when enabling the horizontal propagation. Note that this behavior is only observed above the jet. Globally, the meridional drag accelerates the flow from the winter towards the summer hemisphere for both models (not shown). It remains unclear, however, whether the modeled meridional drag is a consequence of the too strong winter jet over the pole or vice versa. For instance, the ray volume discretization, the interaction with the orographic wave drag parameterization or the structure of

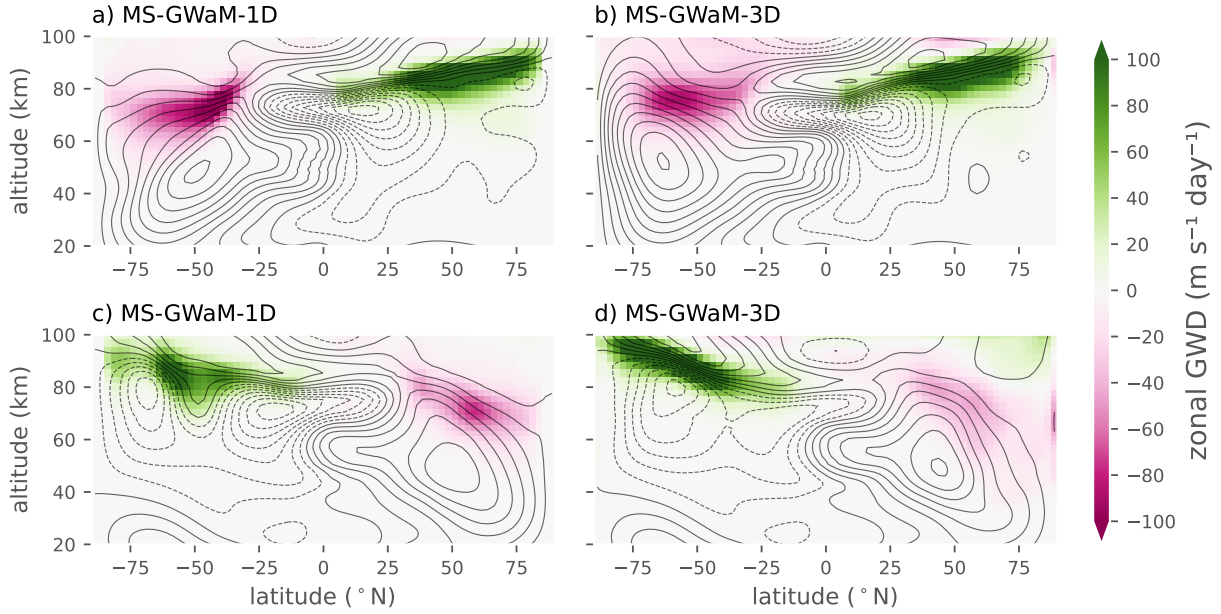


FIG. 7. Zonally averaged zonal gravity wave drag due to the parametrized, non-orographic internal gravity waves. The results are averaged over composites of June (a-b) and December (c-d) 1991 through 1998 and plotted for both MS-GWaM-1D (a, c) and MS-GWaM-3D (b, d). The contours represent the corresponding zonally averaged zonal wind with 10 m s^{-1} increments.

the modeled temperatures may be a cause of the biased wind structures (also compare Sec. 4a and Fig. 2c).^{GSV} Further and more targeted investigation may be needed to bring clarity about this effect.

Differences in^{GSV} refraction behavior can also be seen in the summer hemispheres. However, the model biases of the Northern summer hemispheric jet structures (c.f. Sec. 4a) complicate the interpretation of the wave action budgets in the corresponding regions.

One may now ask the question, how realistic the modeled meridional wave propagation near the Antarctic winter jet is and how it corresponds to satellite observations. To provide some insight,^{GSV} we show the meridional momentum fluxes (cf. Eq. 12) from the composites of June for the years 1991 through 1998 at altitudes $\approx 40 \text{ km}$ ^{GSV} (Fig. 9). Note that the meridional fluxes of MS-GWaM-1D must be interpreted keeping in mind the assumed local horizontal homogeneity. That is, albeit the wave parameters suggest horizontal momentum fluxes, the horizontal propagation (including the wave advection) are set to zero in the columnar setup. The resulting *synthetic* meridional fluxes

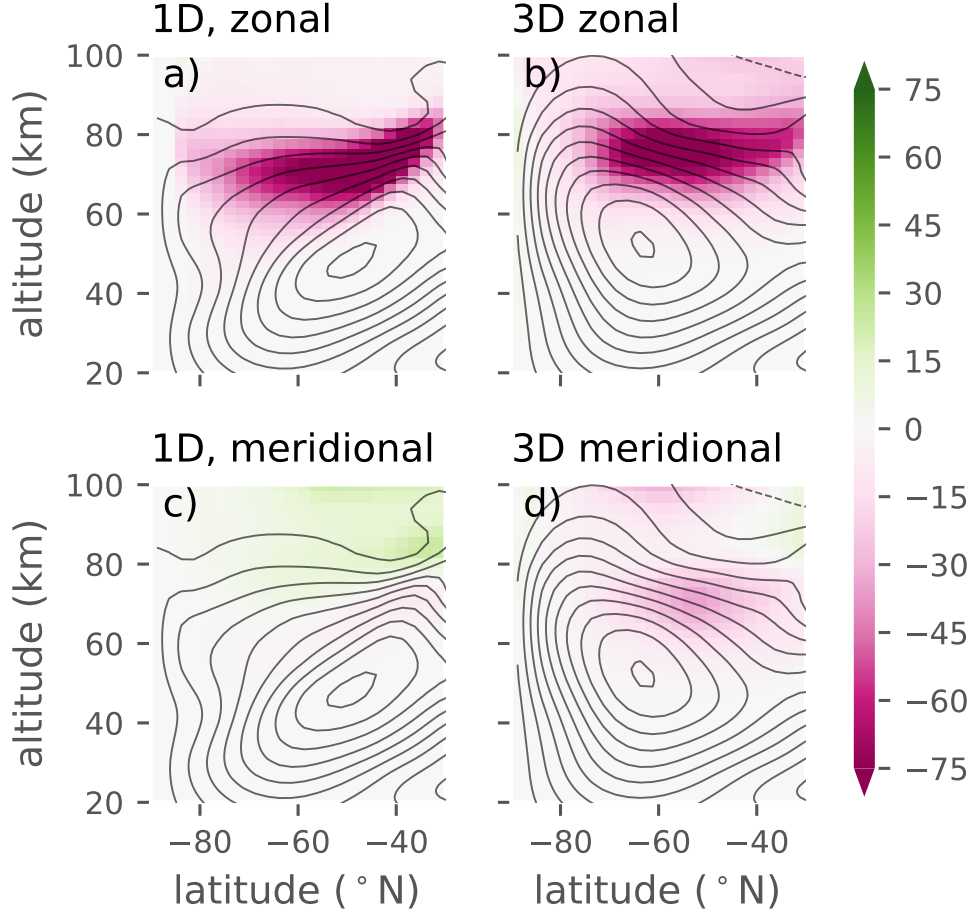


FIG. 8. Zonally averaged zonal gravity wave drag due to the parametrized, non-orographic internal gravity waves. The results are averaged over composites of June (a-b) and December (c-d) 1991 through 1998 and plotted for both MS-GWaM-1D (a, c) and MS-GWaM-3D (b, d). The contours represent the corresponding zonally averaged zonal wind with 10 m s^{-1} increments.

seem to be unrelated to the underlying zonal^{GSV} jet structure (Fig. 9a). As waves are launched homogeneously in all directions at the lower boundary (Sec. 3c) the resulting meridional fluxes are a product of the partial wave filtering due to local vertical gradients of both the horizontal wind and the buoyancy frequency. In contrast, MS-GWaM-3D shows meridional convergence of wave momentum fluxes into the polar jet (Fig. 9b). In particular, the meridional fluxes are northward over the Antarctic continent and southward further north. The change in sign, i.e. the convergence zone, roughly coincides with the zonal wind maximum. This convergence effect of internal gravity waves into the polar night jets is well documented from both observations and general circulation

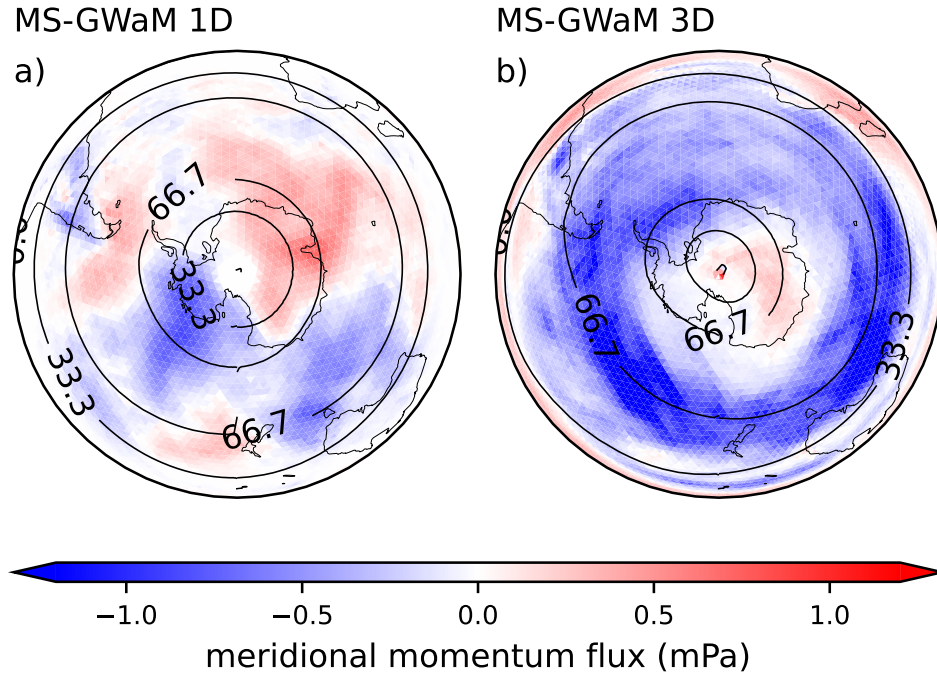


FIG. 9. Meridional momentum fluxes in MS-GWaM-1D (a) and MS-GWaM-3D (b) for composites of Junes from 1991 through 1998 at an altitude of $z \approx 40 \text{ km}^{\text{GSV}}$ overlaid by the corresponding zonal winds (contours, units in m s^{-1}). The maps show the typically observed refraction of internal gravity waves into the Southern polar night jet and modified wind patterns.

models (e.g. Dunkerton and Butchart 1984; Sato et al. 2012; Ehard et al. 2017; Hindley et al. 2020; Gupta et al. 2021). Notably, the structure and amplitudes of the meridional momentum fluxes from MS-GWaM-3D simulations resemble the observations of Hindley et al. (2020, compare their Fig. 3d). Naturally, MS-GWaM cannot reproduce the strong momentum fluxes originating from orographic waves over the Antarctic peninsula, the Southern Andes or the islands of the Southern Ocean. The otherwise fairly close fit, however, gives us high confidence in the correctness of MS-GWaM-3D.^{GSV}

5. Discussion of achievements and challenges

Although internal gravity waves (IGWs) are an essential part of atmospheric dynamics, their parameterization in general circulation models is typically subject to various simplifications. In particular, the single-column assumption, the steady-state approximation, and the balanced mean-flow assumption have usually been made. Here, we present a fully 3-dimensional implementation

of the Multi-Scale Gravity Wave Model, MS-GWaM-3D, which aims at parameterizing IGWs through Lagrangian ray-tracing without the three mentioned assumptions. In general, we find that including 3D transience significantly impacts global IGW propagation patterns and thus horizontal IGW distributions. Correspondingly, the associated wave drag and mean flows are modified.

We compare two distinct situations: For MS-GWaM-1D, where the columnar approximation is applied, the vertical propagation is balanced by wave breaking in the wave action equation (Figs. 4 and 5, panels c and e). Only waves that did not encounter critical layers according to their wave properties may propagate to higher altitudes and eventually break. In contrast, MS-GWaM-3D allows for modulated and spatially unconstrained propagation and enables waves to be refracted around wind structures. As a consequence, both the horizontal and vertical propagation balance with the wave dissipation (Figs. 4 and 5, panels b, d, and f). The equal order of magnitude in the contributions of the horizontal and vertical wave propagation to the wave action budget emphasizes the importance of including horizontal propagation. Moreover, it questions the validity of using columnar methods when, e.g., studying IGW distributions. Both methods do, however, perform as expected in reproducing the cold summer pole and the warm winter pole at altitudes ~ 85 km and ~ 60 km, respectively, in the climatological zonal mean (Fig. 3). The corresponding wind reversals and the mesopause altitudes are reasonably predicted (Fig. 2). We are thus confident that MS-GWaM-3D, as MS-GWaM-1D before it, covers some major effects of IGWs on the mean-flow dynamics, rendering MS-GWaM-3D a viable IGW parameterization. The 3D wave propagation is also found to have significant impacts on the variability of the zonal-mean flow, such as the quasi-biennial oscillation (QBO), as presented by Kim et al. (2023)^{GSV}.

Including the horizontal propagation does, however, also introduce some important differences in the simulated climatology. In particular, the southern hemispheric winter jet becomes stronger near the pole at altitudes 60 to 80 km for MS-GWaM-3D (Fig. 2c). The reason behind this change is, however, not obvious. One possible explanation is the northward refraction of gravity waves^{GSV} near the Antarctic winter jet in MS-GWaM-3D as compared to MS-GWaM-1D. Both the 3D wave action tendencies (dipole structures in Fig. 4d and f) and the zonally averaged wave action fluxes (vectors in Fig. 6a and b) suggest that the 3D modulation causes IGWs to propagate northward and thus relate to a weaker gravity wave drag at high altitudes and similar latitudes (Fig. 8a and b). Additionally, the meridional wave drag near the jet is oppositely directed, that is southward,

for MS-GWaM-3D (Fig. 8c and d). It remains unclear, however, whether the wave refraction and ultimately the wave drag cause the shifts of the jets as the two structures are non-linearly coupled. Possible other causes are the numerical simplifications made in the setup of the ray tracer in the spherical coordinate system or code dependencies of the gravity wave parameterization with other parameterizations, for instance the orographic gravity wave drag. Finally, the jets are sensitive to the structure of the modeled temperature distribution, which in turn is dependent on for instance the ozone climatology and the radiation scheme. A thorough investigation will be needed, and we hope to answer these questions in an envisioned follow-up study. Finally, we find that the meridional wave propagation in MS-GWaM-3D around the Antarctic polar night jet resembles the observations of Hindley et al. (2020) both in amplitudes and structure, up to orographic wave sources such as the Southern Andes (Fig. 9). This gives us high confidence into the implementations as the convergence into the polar night jet is well documented in a number of studies (e.g. Dunkerton and Butchart 1984; Sato et al. 2012; Ehard et al. 2017; Hindley et al. 2020; Gupta et al. 2021).^{GSV}

There is a long list of effects that may be analyzed in more detail from this starting point. Notably, the role of IGWs in sudden stratospheric warmings (e.g. Baldwin et al. 2021), the accuracy of the final warming date (e.g. Cámara et al. 2016; Eichinger et al. 2023), the missing wave drag at 60°S (e.g. Holt et al. 2023), etc. are of interest and are planned for future simulations and analyses. Current investigations include the impact of 3D-transient waves on the quasi-biennial oscillation and wave intermittency. Moreover, there are efforts into increasing the realism of the included IGW sources related to jets-frontal systems and flow over topography. Finally, code optimization may reduce the computational cost which amounts to a runtime factor ~ 30 with respect to runs without any non-orographic wave drag parameterization (c.f. Appendix B5). With these challenges in mind, we ultimately aim for the application of MS-GWaM-3D in climate simulations and possibly numerical weather predictions.

Furthermore, there are numerous potential improvements that may be added to MS-GWaM in the future, albeit not considered here. Most importantly, MS-GWaM-3D—for the time being—does not include a flow-dependent description of the emission of IGWs from jets and fronts (Charron and Manzini 2002; Richter et al. 2010; Cámara and Lott 2015) or flow over topography (Palmer et al. 1986; Bacmeister et al. 1994; Lott and Miller 1997; Xie et al. 2020, 2021; van Niekerk and Vosper 2021; van Niekerk et al. 2023; Eichinger et al. 2023). For the latter reason, MS-GWaM

needs augmentation with a subgrid-scale orography parameterization. Moreover, it is not clear how important modulated triadic resonant interactions among IGWs or between subgrid-scale geostrophic modes and IGWs are for atmospheric dynamics, which could, however, be investigated through ray tracing techniques (c.f. Kafiabad et al. 2019; Voelker et al. 2020).

Acknowledgments. UA thanks the German Research Foundation (DFG) for partial support through the research unit "Multiscale Dynamics of Gravity Waves" (MS-GWaves, grants AC 71/8-2, AC 71/9-2, and AC 71/12-2) and CRC 301 "TPChange" (Project-ID 428312742, Projects B06 "Impact of small-scale dynamics on UTLS transport and mixing" and B07 "Impact of cirrus clouds on tropopause structure"). YHK and UA thank the German Federal Ministry of Education and Research (BMBF) for partial support through the program Role of the Middle Atmosphere in Climate (ROMIC II: QUBICC) and through grant 01LG1905B. UA and GSV thank the German Research Foundation (DFG) for partial support through the CRC 181 "Energy transfers in Atmosphere and Ocean" (Project Number 274762653, Projects W01 "Gravity-wave parameterization for the atmosphere" and S02 "Improved Parameterizations and Numerics in Climate Models."). UA is furthermore grateful for support by Eric and Wendy Schmidt through the Schmidt Futures VESRI "DataWave" project. This work used resources of the Deutsches Klimarechenzentrum (DKRZ) granted by its Scientific Steering Committee (WLA) under project ID bb1097.

Data availability statement. All data used in this publication may be available upon request to the corresponding author.

APPENDIX A

The gravity wave forcing of the mean flow and its relation to the EP-flux formulation

As laid out in Sec. 2, MS-GWaM-3D utilizes the perturbation flux formulation as introduced by Wei et al. (2019). The interested reader may note that the resulting mean flow impact differs from the commonly used pseudomomentum flux convergence related to the Eliassen-Palm flux (Eliassen and Palm 1961; Andrews and McIntyre 1976). To highlight the relation to the latter, we would first like to remind the reader about the underlying assumption of the multiscale theory applied here. Firstly, the theory is built on the compressible Euler equations such that non-linearities not only arise from the advection operators but also from the pressure gradient terms. As MS-GWaM acts as

a gravity wave parameterization for the underlying Eulerian model, phase averages are constructed in a Eulerian sense, accordingly. In terms of scale separation, it is assumed that horizontal scales are much larger than vertical scales. Furthermore, the Brunt-Väisälä frequency is assumed to be much larger than the Coriolis frequency. These assumptions then lead to the regime of small Rossby numbers with a leading order mean-flow in hydrostatic and geostrophic balance. Finally, all wave scales are assumed to be much smaller than the synoptic mean-flow scales.

Under these conditions, the impact of the internal gravity waves on the mean momentum comprises the momentum-flux convergence and an elastic term arising from variations in density and pressure in the compressible atmosphere. In addition, the mean entropy is forced by a wave potential temperature flux convergence. More specifically, the mean flow impact can then be written as^{GSV}

$$\begin{aligned} \partial_t \mathbf{U}|_{IGW} = & -\frac{1}{\bar{\rho}} \nabla \cdot (\bar{\rho} \langle \mathbf{v}' \mathbf{u}' \rangle) \\ & + \frac{f}{g} \mathbf{e}_r \times \langle \mathbf{u}' b' \rangle, \end{aligned} \quad (\text{A1})$$

$$\partial_t \theta|_{IGW} = -\nabla \cdot \langle \mathbf{u}' \theta' \rangle. \quad (\text{A2})$$

with the wave fluxes expressed as^{GSV}

$$\bar{\rho} \langle \mathbf{v}' \mathbf{u}' \rangle = \int \left[\frac{\hat{\omega}^2 \hat{\mathbf{c}}_g \mathbf{k}_h \mathcal{N} + f^2 (\mathbf{e}_r \times \hat{\mathbf{c}}_g) (\mathbf{e}_r \times \mathbf{k}_h \mathcal{N})}{\hat{\omega}^2 - f^2} \right] d^3 k, \quad (\text{A3})$$

$$\langle \mathbf{u}' \theta' \rangle = \int \left[\frac{\bar{\theta}}{g \bar{\rho}} \hat{\mathbf{c}}_{gr} \frac{f \mathcal{N}^2}{\hat{\omega}^2 - f^2} \mathbf{e}_r \times \mathbf{k}_h \mathcal{N} \right] d^3 k, \quad (\text{A4})$$

$$\frac{f}{g} \mathbf{e}_r \times \langle \mathbf{u}' b' \rangle = \frac{f}{\bar{\theta}} \mathbf{e}_r \times \langle \mathbf{u}' \theta' \rangle. \quad (\text{A5})$$

It is now interesting to additionally consider the quasigeostrophic^{UA} potential vorticity evolution in the presence of internal gravity waves. The corresponding prognostic equation reads^{GSV}

$$(\partial_t + \mathbf{U} \cdot \nabla_r) P = -\mathbf{e}_r \cdot \nabla_r \times \left[\frac{1}{\bar{\rho}} \begin{pmatrix} \nabla_r \cdot \mathcal{H} \\ \nabla_r \cdot \mathcal{G} \\ 0 \end{pmatrix} \right], \quad (\text{A6})$$

where $P = \nabla_r^2 \psi + \bar{\rho}^{-1} \partial_z (\bar{\rho} f^2 / N^2 \partial_z \psi)$ is the quasigeostrophic potential vorticity, denoted in terms of the mean-flow stream function, ψ . Note, that the latter relates to the leading-order synoptic-scale wind through $\mathbf{U} = \mathbf{e}_r \times \nabla_r \psi$ and that within geostrophic theory also the thermodynamic fields can be obtained to leading order from the streamfunction. Hence, as long as the mean flow is within the synoptic scaling regime, it is controlled completely by Eq. (A6)^{UA}. Furthermore, we have denoted the horizontal pseudomomentum fluxes, \mathcal{H} and \mathcal{G} , defined by the spectral integral over the phase-space pseudomomentum fluxes, $\mathcal{G} = \int k \hat{c}_g \mathcal{N} d^3 k$ and $\mathcal{H} = \int l \hat{c}_g \mathcal{N} d^3 k$. For a full derivation, we refer the reader to the work of Achatz et al. (2017) and Achatz (2022), a recent summary was given by Achatz et al. (2023).^{GSV} Of interest is now that, *if the mean-flow is in geostrophic and hydrostatic balance*, Eq. (A6) can also be derived from a modified system of mean-flow equations where one replaces^{UA}

$$\bar{\rho} \langle \mathbf{v}' \mathbf{u}' \rangle \rightarrow \int \hat{c}_g \mathbf{k}_h \mathcal{N} d^3 k, \quad (\text{A7})$$

$$\langle \mathbf{u}' b' \rangle = \frac{g}{\theta} \langle \mathbf{u}' \theta' \rangle \rightarrow 0, \quad (\text{A8})$$

and deletes the elastic term. This is the simplification that is most commonly applied in gravity-wave parameterizations: The momentum-flux convergence in the momentum equation is replaced by the convergence of pseudomomentum flux, the elastic term is neglected, and the entropy flux is set to zero. Under the conditions stated the mean flow then follows to leading order the same dynamics as predicted by (A1) and (A2)^{UA}

Since the zonal means of zonal wind and temperature are to a good approximation in geostrophic and hydrostatic balance, we therefore do not find a statistically significant difference in those fields.^{UA} However, Wei et al. (2019) showed that the local^{UA} transient response of the Eulerian phase averaged wind in the presence of a finite amplitude gravity wave packet becomes more accurate when considering the fluxes as denoted in Eqs. (A1) and (A2). We thus implement this formulation but leave the in-depth analysis of the local wind response to an envisioned follow-up study.

APPENDIX B

Details of the numerical implementation

To simulate transient internal gravity waves, MS-GWaM uses a spectral extension of WKB theory (Bretherton 1966; Grimshaw 1975; Achatz et al. 2017; Achatz 2022, and references therein). A Lagrangian approach is employed to solve the equations numerically (Muraschko et al. 2015; Bölöni et al. 2016, 2021; Kim et al. 2021). Therein the 6-dimensional phase space, spanned by position and wave number, is split into small finite-size ray volumes, propagating according to the eikonal equations (Eqs. 3 to 6). They keep their regular shape of rectangles in $(\lambda, \phi, r, k_\lambda, k_\phi, k_r)$ but their extent in all these six directions are allowed to vary in a volume-preserving manner. The wave-action density carried by each ray volume is constant, unless wave breaking leads to the onset of turbulence and hence a decrease in \mathcal{N} . These discrete Lagrangian volumes must, however, be connected to the local Eulerian model state to incorporate direct non-linear interactions between the mean flow and the gravity waves (c.f. Sec. 2 and 3). This coupling poses a number of computational challenges, which are solved as described below.

B1. 3-dimensional field interpolation

When calculating the propagation of a finite-size ray volume in an inhomogeneous medium, it is important to consider that even under the assumption that all wave numbers are constant throughout the volume, the group velocities can differ significantly within the same ray volume. In particular, the scale height correction, Γ , the Brunt-Väisälä frequency, N , and the mean winds, \mathbf{U} , are functions of space and differ between the four faces forming with the meridional and zonal boundaries of the ray volume (see crosses in Fig. B1). To account for a corresponding change in the area of the ray volume, we interpolate all needed background fields horizontally to the face-center positions and the ray volume center through linear Taylor expansions as follows:

$$\chi(\mathbf{r}_j) = \chi(\mathbf{r}_{cc}) + [\nabla_{\mathbf{r}}\chi]_{cc} \cdot (\mathbf{r}_j - \mathbf{r}_{cc}), \quad (\text{B1})$$

where χ symbolizes the interpolated field and the subscripts cc and j refer to evaluations at the cell center and the ray-volume face or ray-volume center, respectively. In the vertical, we apply linear interpolations between the grid points. While the tendencies for the wave numbers are computed with the ray-volume centered values, the interpolated fields at the ray volume faces are used to

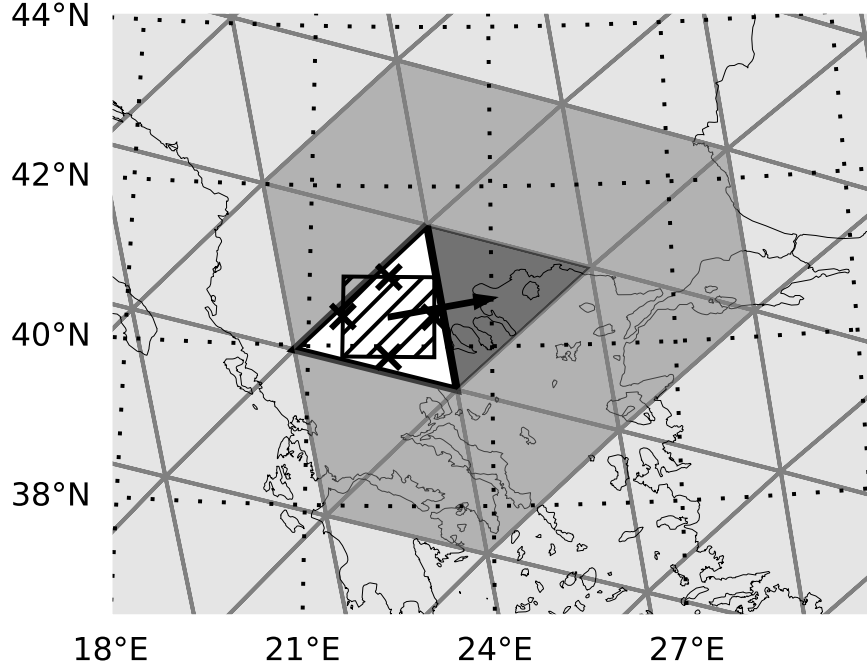


FIG. B1. Sketch of the horizontal extent of a Lagrangian ray volume propagating in the unstructured triangular grid of the ICON model. The propagating ray volume (hatched box) may be associated with a current parent column (framed white grid cell). Given a horizontal group velocity (black arrow) we may expect it to propagate into a neighboring column (dark gray shaded grid cell). The crosses at the edges of the ray volume mark the locations for which background field data is needed to calculate the propagation of the ray volume.

compute group velocities, enabling the prediction of the changing extent of the ray volume in physical space (Eqs. 1 to 2). In particular, the difference in the group velocities at the center of opposing ray-volume faces predicts the rate of compression along the corresponding direction. The average of the opposing group velocities is then used to predict the change of location along the characteristic (Eq. 3). Consequently, the change in the wave number extents $\Delta(k_\lambda, k_\phi, k_r)$ are determined following the procedure described in section 3a.

B2. Horizontal propagation and code parallelization

Since MS-GWaM propagates Lagrangian ray volumes through space, it cannot easily be parallelized using the traditional MPI infrastructure of the ICON model developed for the synchronization of Eulerian fields. In particular, the ray volumes may propagate over large distances and transfer between parallel MPI domains. To accompany this while avoiding load balancing problems, we

associate each ray volume with a parent cell based on its current location and store it in a corresponding grid-based array. As an example, in the shown sketch (Fig. B1) the hatched ray volume is associated with the white-bounded underlying cell. It may, however, have a group velocity such that it propagates into a new parent cell, represented by the arrow and the dark gray shaded triangle, respectively. Therefore, after each propagation step, all cells such as the dark gray shaded triangle search all rays in all neighboring cells (light gray shading) and transfer those that are now located in their own cell area. With this construction, we can localize arrays of ray volumes based on the Eulerian grid column. The integration along the wave characteristics, launch processes, saturation calculations, and wave projection onto the Eulerian grid can then be parallelized using the domain decomposition of the dynamical core with the given model infrastructure. Note that the modulation equations are integrated using a 3-step Runge-Kutta low-storage scheme (Williamson 1980).

B3. Ray volume splitting

In general, the numerical treatment of internal gravity waves as ray volumes is set up to be exact in the limit of infinitesimally small ray volumes and Eulerian grid cells. The actual sizes of both are, however, finite. While the total phase-space volume of the rays is constant by construction, they may stretch or compress either in physical or spectral space. To avoid large numerical artifacts, we therefore split all ray volumes, j , vertically which become larger than the local thresholds

$$\Delta r_j > \max(\alpha_s h_c, 1 \text{ km}), \quad (\text{B2})$$

with the local grid-cell height, h_c , and a scale factor α_s (which is set to 2.5 in this study). The volume is cut into two equally sized ray volumes in the vertical, with the wave vectors identical to the original parent wave. The carrier ray location of each split volume is then set to its center. Similarly, ray volumes are split horizontally where either of the three thresholds is reached

$$\begin{aligned} \cos \phi_j \Delta \lambda_j &> \alpha_s \sqrt{a_c} / R, \\ \Delta \phi_j &> \alpha_s \sqrt{a_c} / R, \end{aligned} \quad (\text{B3})$$

$$\cos \phi_j \Delta \lambda_j \Delta \phi_j > \alpha_s a_c / R^2. \quad (\text{B4})$$

Here, a_c represents the local cell area, and R the Earth mean radius. Splitting is done along the direction of the larger extent.

B4. Horizontal flux smoothing

To avoid numerical artifacts based on the employed simplification in the ray volume representation, we smooth all diagnostic outputs and wave fluxes. Each triangular cell combines three vertices, one in each corner (c.f. Fig. B1). Each of these vertices is connected to five or six neighboring cells, depending on the location of the triangulated icosahedron. The smoothing algorithm first averages the corresponding fields over these pentagons or hexagons and then combines the three resulting values into one average. Consequently, the weights are distributed such that the center cell is weighted with a factor 3, the direct adjacent cells with one common edge are weighted with a factor 2, and all neighboring cells sharing a vertex with the center cell are weighted with a factor 1. While this procedure generally reduces the amplitude of strong flux peaks, it also reduces the occurrence of grid-scale noise and ensures model stability.

B5. Computational performance

Finally, conceptual models need to prove themselves not only through the accurate representation of not-resolved physics but also through competitive performance. In particular, ray-tracing models may suffer from load balancing problems due to the uneven distribution of ray integrations between processors but also the existence of too many rays in general. As described in Sec. B2, MS-GWaM utilizes a cell-based representation of ray volumes which is highly parallelizable such that load balancing problems may not inhibit the model performance. Additionally, the total number of ray volumes is restricted by the maximum numbers $n_{bg} \leq 4800$ and $n_{conv} \leq 8800$ per model-grid column for background and convective gravity waves, respectively. For the lowest impact, the ray volumes with the lowest wave energy are chosen to be removed. Detailed analyses show that the impact of this procedure is indeed small and may be neglected (not shown).

To measure the performance of the model, we compare the runtimes of all two-month runs without any non-orographic gravity wave parameterization with both the MS-GWaM-1D and MS-GWaM-3D setups (Fig. B2). Additionally, we show the fraction of runtime that is associated with MS-GWaM and normalize all values with the number of simulated days. These measures show

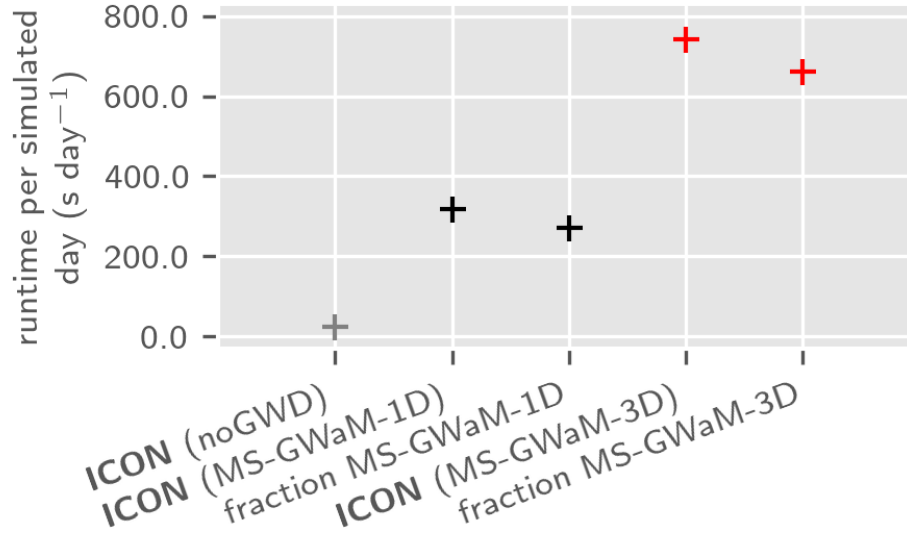


FIG. B2. Performance comparison for UA-ICON at the R2B4 resolution (~ 160 km) parallelized over 1920 MPI cores for runs without IGW parameterization (gray), MS-GWaM-1D (black) and MS-GWaM-3D (red). In addition to the total run time of ICON per simulated day, we show the fraction of run time associated with MS-GWaM-1D and -3D. The median values for the three setups are 25 s d^{-1} , 317 s d^{-1} , and 743 s d^{-1} and thus MS-GWaM-1D and -3D slow down the model by about a factor of 12 and 30, respectively.

that MS-GWaM-1D and MS-GWaM-3D slow down ICON by factors of approximately 12 and 30, respectively. That is, the 3D setup has a performance penalty equal to a factor of approximately 2.5. Still, the gravity wave parameterization is several orders of magnitude faster than wave-resolving simulations - for which Bölöni et al. (2021) estimate a cost factor of about six orders of magnitude - and thus a competitive tool for the estimate and analysis of global IGW effects.

References

Achatz, U., 2022: *Atmospheric Dynamics*. 1st ed., Springer Berlin Heidelberg, URL <https://link.springer.com/book/9783662639429>.

Achatz, U., Y.-H. Kim, and G. S. Voelker, 2023: Multi-scale dynamics of the interaction between waves and mean flows: From nonlinear WKB theory to gravity-wave parameterizations in weather and climate models. *Journal of Mathematical Physics*, **64** (11), 111 101, <https://doi.org/10.1063/5.0165180>, URL <https://doi.org/10.1063/5.0165180>.

- Achatz, U., R. Klein, and F. Senf, 2010: Gravity waves, scale asymptotics and the pseudo-incompressible equations. *Journal of Fluid Mechanics*, **663**, 120–147, <https://doi.org/10.1017/S0022112010003411>, URL http://www.journals.cambridge.org/abstract_S0022112010003411, publisher: Cambridge University Press.
- Achatz, U., B. Ribstein, F. Senf, and R. Klein, 2017: The interaction between synoptic-scale balanced flow and a finite-amplitude mesoscale wave field throughout all atmospheric layers: weak and moderately strong stratification. *Quarterly Journal of the Royal Meteorological Society*, **143 (702)**, 342–361, <https://doi.org/10.1002/qj.2926>.
- Alexander, M. J., and T. J. Dunkerton, 1999: A Spectral Parameterization of Mean-Flow Forcing due to Breaking Gravity Waves. *Journal of the Atmospheric Sciences*, **56 (24)**, 4167–4182, [https://doi.org/10.1175/1520-0469\(1999\)056<4167:ASPOMF>2.0.CO;2](https://doi.org/10.1175/1520-0469(1999)056<4167:ASPOMF>2.0.CO;2), URL https://journals.ametsoc.org/view/journals/atsc/56/24/1520-0469_1999_056_4167_aspomf_2.0.co_2.xml, publisher: American Meteorological Society Section: Journal of the Atmospheric Sciences.
- Alexander, M. J., and Coauthors, 2010: Recent developments in gravity-wave effects in climate models and the global distribution of gravity-wave momentum flux from observations and models. *Quarterly Journal of the Royal Meteorological Society*, **136 (650)**, 1103–1124, <https://doi.org/10.1002/qj.637>, URL <https://onlinelibrary.wiley.com/doi/abs/10.1002/qj.637>, eprint: <https://onlinelibrary.wiley.com/doi/pdf/10.1002/qj.637>.
- Amemiya, A., and K. Sato, 2016: A New Gravity Wave Parameterization Including Three-Dimensional Propagation. *Journal of the Meteorological Society of Japan. Ser. II*, **94 (3)**, 237–256, <https://doi.org/10.2151/jmsj.2016-013>.
- Andrews, D. G., and M. E. McIntyre, 1976: Planetary Waves in Horizontal and Vertical Shear: The Generalized Eliassen-Palm Relation and the Mean Zonal Acceleration. *Journal of the Atmospheric Sciences*, **33 (11)**, 2031–2048, [https://doi.org/10.1175/1520-0469\(1976\)033<2031:PWIHAV>2.0.CO;2](https://doi.org/10.1175/1520-0469(1976)033<2031:PWIHAV>2.0.CO;2), URL <http://journals.ametsoc.org/doi/abs/10.1175/1520-0469%281976%29033%3C2031%3APWIHAV%3E2.0.CO%3B2>, ISBN: 0022492815200469.
- Bacmeister, J. T., P. A. Newman, B. L. Gary, and K. R. Chan, 1994: An Algorithm for Forecasting Mountain Wave-Related Turbulence in the Stratosphere. *Weather and Forecast-*

- ing*, **9** (2), 241–253, [https://doi.org/10.1175/1520-0434\(1994\)009<0241:AAFFMW>2.0.CO;2](https://doi.org/10.1175/1520-0434(1994)009<0241:AAFFMW>2.0.CO;2), URL https://journals.ametsoc.org/view/journals/wefo/9/2/1520-0434_1994_009_0241_aaffmw_2.0_co_2.xml, publisher: American Meteorological Society Section: Weather and Forecasting.
- Baldwin, M. P., and Coauthors, 2021: Sudden Stratospheric Warmings. *Reviews of Geophysics*, **59** (1), e2020RG000708, <https://doi.org/10.1029/2020RG000708>, URL <https://onlinelibrary.wiley.com/doi/abs/10.1029/2020RG000708>, eprint: <https://onlinelibrary.wiley.com/doi/pdf/10.1029/2020RG000708>.
- Borchert, S., G. Zhou, M. Baldauf, H. Schmidt, G. Zängl, and D. Reinert, 2019: The upper-atmosphere extension of the ICON general circulation model (version: Ua-icon-1.0). *Geoscientific Model Development*, **12** (8), 3541–3569, <https://doi.org/10.5194/gmd-12-3541-2019>, URL <https://doi.org/10.5194/gmd-12-3541-2019>.
- Bretherton, F. P., 1966: The propagation of groups of internal gravity waves in a shear flow. *Quarterly Journal of the Royal Meteorological Society*, **92** (394), 466–480, <https://doi.org/10.1002/qj.49709239403>, URL <http://doi.wiley.com/10.1002/qj.49709239403>, publisher: John Wiley & Sons, Ltd.
- Bölöni, G., Y.-H. Kim, S. Borchert, and U. Achatz, 2021: Toward Transient Subgrid-Scale Gravity Wave Representation in Atmospheric Models. Part I: Propagation Model Including Nondissipative Wave–Mean-Flow Interactions. *Journal of the Atmospheric Sciences*, **78** (4), 1317–1338, <https://doi.org/10.1175/JAS-D-20-0065.1>, URL <https://journals.ametsoc.org/view/journals/atsc/78/4/JAS-D-20-0065.1.xml>, publisher: American Meteorological Society Section: Journal of the Atmospheric Sciences.
- Bölöni, G., B. Ribstein, J. Muraschko, C. Sgoff, J. Wei, and U. Achatz, 2016: The Interaction between Atmospheric Gravity Waves and Large-Scale Flows: An Efficient Description beyond the Nonacceleration Paradigm. *Journal of the Atmospheric Sciences*, **73** (12), 4833–4852, <https://doi.org/10.1175/JAS-D-16-0069.1>, URL <http://journals.ametsoc.org/doi/10.1175/JAS-D-16-0069.1>.
- Charron, M., and E. Manzini, 2002: Gravity Waves from Fronts: Parameterization and Middle Atmosphere Response in a General Circulation Model. *Journal of the Atmospheric*

- Sciences*, **59** (5), 923–941, [https://doi.org/10.1175/1520-0469\(2002\)059<0923:GWFFPA>2.0.CO;2](https://doi.org/10.1175/1520-0469(2002)059<0923:GWFFPA>2.0.CO;2), URL https://journals.ametsoc.org/view/journals/atsc/59/5/1520-0469_2002_059_0923_gwffpa.2.0.co_2.xml, publisher: American Meteorological Society Section: Journal of the Atmospheric Sciences.
- Cámara, A. d. I., and F. Lott, 2015: A parameterization of gravity waves emitted by fronts and jets. *Geophysical Research Letters*, **42** (6), 2071–2078, <https://doi.org/10.1002/2015GL063298>, URL <https://onlinelibrary.wiley.com/doi/abs/10.1002/2015GL063298>, eprint: <https://onlinelibrary.wiley.com/doi/pdf/10.1002/2015GL063298>.
- Cámara, A. d. I., F. Lott, V. Jewtoukoff, R. Plougonven, and A. Hertzog, 2016: On the Gravity Wave Forcing during the Southern Stratospheric Final Warming in LMDZ. *Journal of the Atmospheric Sciences*, **73** (8), 3213–3226, <https://doi.org/10.1175/JAS-D-15-0377.1>, URL <https://journals.ametsoc.org/view/journals/atsc/73/8/jas-d-15-0377.1.xml>, publisher: American Meteorological Society Section: Journal of the Atmospheric Sciences.
- Drob, D. P., and Coauthors, 2015: An update to the Horizontal Wind Model (HWM): The quiet time thermosphere. *Earth and Space Science*, **2** (7), 301–319, <https://doi.org/10.1002/2014EA000089>, URL <https://agupubs.onlinelibrary.wiley.com/doi/10.1002/2014EA000089>.
- Dunkerton, T. J., and N. Butchart, 1984: Propagation and selective transmission of internal gravity waves in a sudden warming. *Journal of the Atmospheric Sciences*, **41** (8), 1443–1460, [https://doi.org/10.1175/1520-0469\(1984\)041<1443:PASTOI>2.0.CO;2](https://doi.org/10.1175/1520-0469(1984)041<1443:PASTOI>2.0.CO;2), URL https://journals.ametsoc.org/view/journals/atsc/41/8/1520-0469_1984_041_1443_pastoi_2_0_co_2.xml, publisher: American Meteorological Society.
- Ehard, B., and Coauthors, 2017: Horizontal propagation of large-amplitude mountain waves into the polar night jet. *Journal of Geophysical Research: Atmospheres*, **122** (3), 1423–1436, <https://doi.org/10.1002/2016JD025621>, URL <https://onlinelibrary.wiley.com/doi/abs/10.1002/2016JD025621>, eprint: <https://onlinelibrary.wiley.com/doi/pdf/10.1002/2016JD025621>.
- Eichinger, R., and Coauthors, 2023: Emulating lateral gravity wave propagation in a global chemistry–climate model (EMAC v2.55.2) through horizontal flux redistribution. *Geoscientific*

- Model Development*, **16 (19)**, 5561–5583, <https://doi.org/10.5194/gmd-16-5561-2023>, URL <https://gmd.copernicus.org/articles/16/5561/2023/>, publisher: Copernicus GmbH.
- Eliassen, A., and E. Palm, 1961: On the transfer of energy in stationary mountain waves. *Geofysiske Publikasjoner*, **22 (3)**, 1–23, URL http://www.ngfweb.no/geophysica_norvegica.html#22.
- Emmert, J. T., and Coauthors, 2021: NRLMSIS 2.0: A Whole-Atmosphere Empirical Model of Temperature and Neutral Species Densities. *Earth and Space Science*, **8 (3)**, e2020EA001321, <https://doi.org/10.1029/2020EA001321>, URL <https://onlinelibrary.wiley.com/doi/abs/10.1029/2020EA001321>, eprint: <https://onlinelibrary.wiley.com/doi/pdf/10.1029/2020EA001321>.
- Emmert, J. T., and Coauthors, 2022: NRLMSIS 2.1: An Empirical Model of Nitric Oxide Incorporated Into MSIS. *Journal of Geophysical Research: Space Physics*, **127 (10)**, <https://doi.org/10.1029/2022JA030896>, publisher: John Wiley and Sons Inc.
- Ern, M., Q. T. Trinh, P. Preusse, J. C. Gille, M. G. Mlynczak, J. M. Russell III, and M. Riese, 2018: GRACILE: a comprehensive climatology of atmospheric gravity wave parameters based on satellite limb soundings. *Earth System Science Data*, **10 (2)**, 857–892, <https://doi.org/10.5194/essd-10-857-2018>, URL <https://essd.copernicus.org/articles/10/857/2018/>, publisher: Copernicus GmbH.
- Fritts, D. C., and M. J. Alexander, 2003: Gravity wave dynamics and effects in the middle atmosphere. *Reviews of Geophysics*, **41 (1)**, 1/1003, <https://doi.org/10.1029/2001RG000106>, URL <http://doi.wiley.com/10.1029/2001RG000106>, publisher: Wiley-Blackwell.
- Grimshaw, R., 1974: Internal gravity waves in a slowly varying, dissipative medium. *Geophysical Fluid Dynamics*, **6 (2)**, 131–148, <https://doi.org/10.1080/03091927409365792>, URL <https://www.tandfonline.com/doi/abs/10.1080/03091927409365792>, publisher: Informa UK Limited.
- Grimshaw, R., 1975: Nonlinear internal gravity waves in a rotating fluid. *Journal of Fluid Mechanics*, **71 (3)**, 497–512, <https://doi.org/10.1017/S0022112075002704>, publisher: Cambridge University Press.
- Gupta, A., T. Birner, A. Dörnbrack, and I. Polichtchouk, 2021: Importance of Gravity Wave Forcing for Springtime Southern Polar Vortex Breakdown as Revealed by ERA5. *Geophysical Research Letters*, **48 (10)**, <https://doi.org/10.1029/2021GL092762>.

- Hasha, A., O. Bühler, and J. Scinocca, 2008: Gravity Wave Refraction by Three-Dimensionally Varying Winds and the Global Transport of Angular Momentum. *Journal of the Atmospheric Sciences*, **65**, 2892–2906, <https://doi.org/10.1175/2007JAS2561.1>.
- Hindley, N. P., C. J. Wright, L. Hoffmann, T. Moffat-Griffin, and N. J. Mitchell, 2020: An 18-Year Climatology of Directional Stratospheric Gravity Wave Momentum Flux From 3-D Satellite Observations. *Geophysical Research Letters*, **47** (22), <https://doi.org/10.1029/2020GL089557>, publisher: Blackwell Publishing Ltd.
- Hines, C. O., 1997a: Doppler-spread parameterization of gravity-wave momentum deposition in the middle atmosphere. Part 1: Basic formulation. *Journal of Atmospheric and Solar-Terrestrial Physics*, **59** (4), 371–386, [https://doi.org/10.1016/S1364-6826\(96\)00079-X](https://doi.org/10.1016/S1364-6826(96)00079-X), URL <https://www.sciencedirect.com/science/article/pii/S136468269600079X>.
- Hines, C. O., 1997b: Doppler-spread parameterization of gravity-wave momentum deposition in the middle atmosphere. Part 2: Broad and quasi monochromatic spectra, and implementation. *Journal of Atmospheric and Solar-Terrestrial Physics*, **59** (4), 387–400, [https://doi.org/10.1016/S1364-6826\(96\)00080-6](https://doi.org/10.1016/S1364-6826(96)00080-6), URL <https://www.sciencedirect.com/science/article/pii/S1364682696000806>.
- Holt, L. A., M. J. Alexander, L. Coy, A. Molod, W. Putman, and S. Pawson, 2016: Tropical Waves and the Quasi-Biennial Oscillation in a 7-km Global Climate Simulation. *Journal of the Atmospheric Sciences*, **73** (9), 3771–3783, <https://doi.org/10.1175/JAS-D-15-0350.1>, URL <https://journals.ametsoc.org/view/journals/atsc/73/9/jas-d-15-0350.1.xml>, publisher: American Meteorological Society Section: Journal of the Atmospheric Sciences.
- Holt, L. A., C. M. Brabec, and M. J. Alexander, 2023: Exploiting High-Density Zonal-Sampling of HIRDLS Profiles Near 60°S to Investigate Missing Drag in Chemistry-Climate Models. *Journal of Geophysical Research: Atmospheres*, **128** (8), e2022JD037398, <https://doi.org/10.1029/2022JD037398>, URL <https://onlinelibrary.wiley.com/doi/abs/10.1029/2022JD037398>, eprint: <https://onlinelibrary.wiley.com/doi/pdf/10.1029/2022JD037398>.
- Jiang, J. H., S. D. Eckermann, D. L. Wu, and D. Y. Wang, 2006: Inter-annual variation of gravity waves in the Arctic and Antarctic winter middle atmosphere. *Advances in Space Research*,

38 (11), 2418–2423, <https://doi.org/10.1016/j.asr.2005.09.036>, URL <https://www.sciencedirect.com/science/article/pii/S027311770501121X>.

Kafiabad, H. A., M. A. Savva, and J. Vanneste, 2019: Diffusion of inertia-gravity waves by geostrophic turbulence. *Journal of Fluid Mechanics*, **869**, <https://doi.org/10.1017/jfm.2019.300>, publisher: Cambridge University Press.

Kim, Y. H., G. Bölöni, S. Borchert, H. Y. Chun, and U. Achatz, 2021: Toward transient subgrid-scale gravity wave representation in atmospheric models. Part II: Wave intermittency simulated with convective sources. *Journal of the Atmospheric Sciences*, **78 (4)**, 1339–1357, <https://doi.org/10.1175/JAS-D-20-0066.1>, URL <https://journals.ametsoc.org/view/journals/atsc/aop/JAS-D-20-0066.1/JAS-D-20-0066.1.xml>, publisher: American Meteorological Society.

Kim, Y.-H., G. S. Voelker, G. Bölöni, G. Zängl, and U. Achatz, 2023: Crucial role of obliquely propagating gravity waves in the quasi-biennial oscillation dynamics. *EGUsphere*, 1–18, <https://doi.org/10.5194/egusphere-2023-2663>, URL <https://egusphere.copernicus.org/preprints/2023/egusphere-2023-2663/>, publisher: Copernicus GmbH.

Kim, Y.-J., S. D. Eckermann, and H. Y. Chun, 2003: An overview of the past, present and future of gravity-wave drag parametrization for numerical climate and weather prediction models. *Atmosphere - Ocean*, **41 (1)**, 65–98, <https://doi.org/10.3137/ao.410105>, URL <https://www.tandfonline.com/doi/abs/10.3137/ao.410105>, publisher: Taylor & Francis Group.

Kruse, C. G., and Coauthors, 2022: Observed and Modeled Mountain Waves from the Surface to the Mesosphere near the Drake Passage. *Journal of the Atmospheric Sciences*, **79 (4)**, 909–932, <https://doi.org/10.1175/JAS-D-21-0252.1>, URL <https://journals.ametsoc.org/view/journals/atsc/79/4/JAS-D-21-0252.1.xml>, publisher: American Meteorological Society Section: Journal of the Atmospheric Sciences.

Lindzen, R. S., 1981: Turbulence and stress owing to gravity wave and tidal breakdown. *Journal of Geophysical Research*, **86 (C10)**, 9707–9714, <https://doi.org/10.1029/jc086ic10p09707>, publisher: American Geophysical Union (AGU).

- Lott, F., and L. Guez, 2013: A stochastic parameterization of the gravity waves due to convection and its impact on the equatorial stratosphere. *Journal of Geophysical Research: Atmospheres*, **118** (16), 8897–8909, <https://doi.org/10.1002/jgrd.50705>, URL <https://onlinelibrary.wiley.com/doi/abs/10.1002/jgrd.50705>, eprint: <https://onlinelibrary.wiley.com/doi/pdf/10.1002/jgrd.50705>.
- Lott, F., and M. J. Miller, 1997: A new subgrid-scale orographic drag parametrization: Its formulation and testing. *Quarterly Journal of the Royal Meteorological Society*, **123** (537), 101–127, <https://doi.org/10.1002/qj.49712353704>, URL <https://onlinelibrary.wiley.com/doi/abs/10.1002/qj.49712353704>, eprint: <https://onlinelibrary.wiley.com/doi/pdf/10.1002/qj.49712353704>.
- Marks, C. J., and S. D. Eckermann, 1995: A Three-Dimensional Nonhydrostatic Ray Tracing Model for Gravity Waves: Formulation and Preliminary Results for the Middle Atmosphere. *Journal of Atmospheric Sciences*, **52** (11), 1959–1984, ISBN: 9789896540821.
- Medvedev, A. S., and G. P. Klaassen, 1995: Vertical evolution of gravity wave spectra and the parameterization of associated wave drag. *Journal of Geophysical Research: Atmospheres*, **100** (D12), 25 841–25 853, <https://doi.org/10.1029/95JD02533>, URL <https://onlinelibrary.wiley.com/doi/abs/10.1029/95JD02533>, eprint: <https://onlinelibrary.wiley.com/doi/pdf/10.1029/95JD02533>.
- Muraschko, J., M. D. Fruman, U. Achatz, S. Hickel, and Y. Toledo, 2015: On the application of Wentzel-Kramer-Brillouin theory for the simulation of the weakly nonlinear dynamics of gravity waves. *Quarterly Journal of the Royal Meteorological Society*, **141** (688), 676–697, <https://doi.org/10.1002/qj.2381>, URL <http://doi.wiley.com/10.1002/qj.2381>, publisher: John Wiley & Sons, Ltd.
- Nappo, C. J., 2013: *An Introduction to Atmospheric Gravity Waves*. Academic Press.
- Orr, A., P. Bechtold, J. Scinocca, M. Ern, and M. Janiskova, 2010: Improved middle atmosphere climate and forecasts in the ECMWF model through a nonorographic gravity wave drag parameterization. *Journal of Climate*, **23** (22), 5905–5926, <https://doi.org/10.1175/2010JCLI3490.1>, URL <https://journals.ametsoc.org/view/journals/clim/23/22/2010jcli3490.1.xml>, publisher: American Meteorological Society.

- Palmer, T. N., G. J. Shutts, and R. Swinbank, 1986: Alleviation of a systematic westerly bias in general circulation and numerical weather prediction models through an orographic gravity wave drag parametrization. *Quarterly Journal of the Royal Meteorological Society*, **112** (474), 1001–1039, <https://doi.org/10.1002/qj.49711247406>, URL <https://onlinelibrary.wiley.com/doi/abs/10.1002/qj.49711247406>, _eprint: <https://onlinelibrary.wiley.com/doi/pdf/10.1002/qj.49711247406>.
- Polichtchouk, I., A. v. Niekerk, and N. Wedi, 2023: Resolved Gravity Waves in the Extratropical Stratosphere: Effect of Horizontal Resolution Increase from O(10) to O(1) km. *Journal of the Atmospheric Sciences*, **80** (2), 473–486, <https://doi.org/10.1175/JAS-D-22-0138.1>, URL <https://journals.ametsoc.org/view/journals/atsc/80/2/JAS-D-22-0138.1.xml>, publisher: American Meteorological Society Section: Journal of the Atmospheric Sciences.
- Polichtchouk, I., N. Wedi, and Y.-H. Kim, 2022: Resolved gravity waves in the tropical stratosphere: Impact of horizontal resolution and deep convection parametrization. *Quarterly Journal of the Royal Meteorological Society*, **148** (742), 233–251, <https://doi.org/10.1002/qj.4202>, URL <https://onlinelibrary.wiley.com/doi/abs/10.1002/qj.4202>, _eprint: <https://onlinelibrary.wiley.com/doi/pdf/10.1002/qj.4202>.
- Quinn, B., C. Eden, and D. Olbers, 2020: Application of the idemix concept for internal gravity waves in the atmosphere. *Journal of the Atmospheric Sciences*, **77** (10), 3601–3618, <https://doi.org/10.1175/JAS-D-20-0107.1>, publisher: American Meteorological Society.
- Ribstein, B., and U. Achatz, 2016: The interaction between gravity waves and solar tides in a linear tidal model with a 4-D ray-tracing gravity-wave parameterization. *Journal of Geophysical Research A: Space Physics*, **121** (9), 8936–8950, <https://doi.org/10.1002/2016JA022478>.
- Ribstein, B., U. Achatz, and F. Senf, 2015: The interaction between gravity waves and solar tides: Results from 4-D ray tracing coupled to a linear tidal model. *Journal of Geophysical Research A: Space Physics*, **120** (8), 6795–6817, <https://doi.org/10.1002/2015JA021349>.
- Richter, J. H., F. Sassi, and R. R. Garcia, 2010: Toward a Physically Based Gravity Wave Source Parameterization in a General Circulation Model. *Journal of the Atmospheric Sciences*, **67** (1), 136–156, <https://doi.org/10.1175/2009JAS3112.1>, URL <https://journals.ametsoc.org/view/journals/>

atsc/67/1/2009jas3112.1.xml, publisher: American Meteorological Society Section: Journal of the Atmospheric Sciences.

Sacha, P., F. Lilienthal, C. Jacobi, and P. Pisoft, 2016: Influence of the spatial distribution of gravity wave activity on the middle atmospheric dynamics. *Atmospheric Chemistry and Physics*, **16** (24), 15 755–15 775, <https://doi.org/10.5194/acp-16-15755-2016>, URL <https://acp.copernicus.org/articles/16/15755/2016/acp-16-15755-2016.html>, publisher: Copernicus GmbH.

Sato, K., S. Tateno, S. Watanabe, and Y. Kawatani, 2012: Gravity Wave Characteristics in the Southern Hemisphere Revealed by a High-Resolution Middle-Atmosphere General Circulation Model. *Journal of the Atmospheric Sciences*, **69** (4), 1378–1396, <https://doi.org/10.1175/JAS-D-11-0101.1>, URL <https://journals.ametsoc.org/view/journals/atsc/69/4/jas-d-11-0101.1.xml>, publisher: American Meteorological Society Section: Journal of the Atmospheric Sciences.

Sato, K., S. Watanabe, Y. Kawatani, Y. Tomikawa, K. Miyazaki, and M. Takahashi, 2009: On the origins of mesospheric gravity waves. *Geophysical Research Letters*, **36** (19), <https://doi.org/10.1029/2009GL039908>, URL <https://onlinelibrary.wiley.com/doi/abs/10.1029/2009GL039908>, eprint: <https://onlinelibrary.wiley.com/doi/pdf/10.1029/2009GL039908>.

Scaife, A. A., J. R. Knight, G. K. Vallis, and C. K. Folland, 2005: A stratospheric influence on the winter NAO and North Atlantic surface climate. *Geophysical Research Letters*, **32** (18), <https://doi.org/10.1029/2005GL023226>, URL <https://onlinelibrary.wiley.com/doi/abs/10.1029/2005GL023226>, eprint: <https://onlinelibrary.wiley.com/doi/pdf/10.1029/2005GL023226>.

Scaife, A. A., and Coauthors, 2012: Climate change projections and stratosphere–troposphere interaction. *Climate Dynamics*, **38** (9), 2089–2097, <https://doi.org/10.1007/s00382-011-1080-7>, URL <https://doi.org/10.1007/s00382-011-1080-7>.

Scinocca, J. F., 2003: An Accurate Spectral Nonorographic Gravity Wave Drag Parameterization for General Circulation Models. *Journal of the Atmospheric Sciences*, **60** (4), 667–682, [https://doi.org/10.1175/1520-0469\(2003\)060<0667:AASNGW>2.0.CO;2](https://doi.org/10.1175/1520-0469(2003)060<0667:AASNGW>2.0.CO;2), URL https://journals.ametsoc.org/view/journals/atsc/60/4/1520-0469_2003_060_0667_aasngw_

2.0.co.2.xml, publisher: American Meteorological Society Section: Journal of the Atmospheric Sciences.

Sigmond, M., and J. F. Scinocca, 2010: The Influence of the Basic State on the Northern Hemisphere Circulation Response to Climate Change. *Journal of Climate*, **23** (6), 1434–1446, <https://doi.org/10.1175/2009JCLI3167.1>, URL <https://journals.ametsoc.org/view/journals/clim/23/6/2009jcli3167.1.xml>, publisher: American Meteorological Society Section: Journal of Climate.

Sutherland, B. R., 2010: *Internal Gravity Waves*. Cambridge University Press, Cambridge, UK, URL <http://www.cambridge.org/de/academic/subjects/earth-and-environmental-science/atmospheric-science-and-meteorology/internal-gravity-waves?format=HB>.

Sutherland, B. R., U. Achatz, C. C. P. Caulfield, and J. M. Klymak, 2019: Recent progress in modeling imbalance in the atmosphere and ocean. *Physical Review Fluids*, **4** (1), 10 501, <https://doi.org/10.1103/PhysRevFluids.4.010501>.

van Niekerk, A., and S. Vosper, 2021: Towards a more “scale-aware” orographic gravity wave drag parametrization: Description and initial testing. *Quarterly Journal of the Royal Meteorological Society*, **147** (739), 3243–3262, <https://doi.org/10.1002/qj.4126>, URL <https://onlinelibrary.wiley.com/doi/abs/10.1002/qj.4126>, eprint: <https://onlinelibrary.wiley.com/doi/pdf/10.1002/qj.4126>.

van Niekerk, A., S. Vosper, and M. Teixeira, 2023: Accounting for the three-dimensional nature of mountain waves: Parametrising partial critical-level filtering. *Quarterly Journal of the Royal Meteorological Society*, **149** (751), 515–536, <https://doi.org/10.1002/qj.4421>, URL <https://onlinelibrary.wiley.com/doi/abs/10.1002/qj.4421>, eprint: <https://onlinelibrary.wiley.com/doi/pdf/10.1002/qj.4421>.

Voelker, G. S., T. R. Akylas, and U. Achatz, 2020: An application of WKBJ theory for triad interactions of internal gravity waves in varying background flows. *Quarterly Journal of the Royal Meteorological Society*, qj.3962, <https://doi.org/10.1002/qj.3962>, URL <https://onlinelibrary.wiley.com/doi/10.1002/qj.3962>, publisher: John Wiley and Sons Ltd.

Warner, C. D., and M. E. McIntyre, 1996: On the Propagation and Dissipation of Gravity Wave Spectra through a Realistic Middle Atmosphere. *Journal of the Atmospheric Sciences*,

- 53 (22)**, 3213–3235, [https://doi.org/10.1175/1520-0469\(1996\)053<3213:OTPADO>2.0.CO;2](https://doi.org/10.1175/1520-0469(1996)053<3213:OTPADO>2.0.CO;2), URL https://journals.ametsoc.org/view/journals/atsc/53/22/1520-0469_1996_053_3213_otpado_2.0_co_2.xml, publisher: American Meteorological Society Section: Journal of the Atmospheric Sciences.
- Warner, C. D., and M. E. McIntyre, 2001: An Ultrasimple Spectral Parameterization for Nonorographic Gravity Waves. *Journal of the Atmospheric Sciences*, **58 (14)**, 1837–1857, [https://doi.org/10.1175/1520-0469\(2001\)058<1837:AUSPFN>2.0.CO;2](https://doi.org/10.1175/1520-0469(2001)058<1837:AUSPFN>2.0.CO;2), URL https://journals.ametsoc.org/view/journals/atsc/58/14/1520-0469_2001_058_1837_auspfn_2.0_co_2.xml, publisher: American Meteorological Society Section: Journal of the Atmospheric Sciences.
- Wei, J., G. Bölöni, and U. Achatz, 2019: Efficient modeling of the interaction of mesoscale gravity waves with unbalanced large-scale flows: Pseudomomentum-Flux Convergence versus Direct Approach. *Journal of the Atmospheric Sciences*, **76 (9)**, 2715–2738, <https://doi.org/10.1175/JAS-D-18-0337.1>, URL www.ametsoc.org/PUBSReuseLicenses.
- Wilhelm, J., T. R. Akylas, G. Bölöni, J. Wei, B. Ribstein, R. Klein, and U. Achatz, 2018: Interactions between Meso- and Sub-Mesoscale GravityWaves and their Efficient Representation in Mesoscale-Resolving Models. *Journal of the Atmospheric Sciences*, **75**, 2257–2280, <https://doi.org/10.1175/JAS-D-17-0289.1>, URL <http://journals.ametsoc.org/doi/10.1175/JAS-D-17-0289.1>.
- Williams, P. D., and Coauthors, 2017: A Census of Atmospheric Variability From Seconds to Decades. *Geophysical Research Letters*, **44 (21)**, 11,201–11,211, <https://doi.org/10.1002/2017GL075483>, URL <https://onlinelibrary.wiley.com/doi/abs/10.1002/2017GL075483>, eprint: <https://onlinelibrary.wiley.com/doi/pdf/10.1002/2017GL075483>.
- Williamson, J. H., 1980: Low-storage Runge-Kutta schemes. *Journal of Computational Physics*, **35 (1)**, 48–56, [https://doi.org/10.1016/0021-9991\(80\)90033-9](https://doi.org/10.1016/0021-9991(80)90033-9), URL <https://www.sciencedirect.com/science/article/pii/0021999180900339>.
- Xie, J., M. Zhang, Z. Xie, H. Liu, Z. Chai, J. He, and H. Zhang, 2020: An Orographic-Drag Parametrization Scheme Including Orographic Anisotropy for All Flow Directions. *Journal of Advances in Modeling Earth Systems*, **12 (3)**, e2019MS001921, <https://doi.org/10.1029/2019MS001921>.

2019MS001921, URL <https://onlinelibrary.wiley.com/doi/abs/10.1029/2019MS001921>, _eprint: <https://onlinelibrary.wiley.com/doi/pdf/10.1029/2019MS001921>.

Xie, J., M. Zhang, Q. Zeng, Z. Xie, H. Liu, Z. Chai, J. He, and H. Zhang, 2021: Implementation of an Orographic Drag Scheme Considering Orographic Anisotropy in All Flow Directions in the Earth System Model CAS-ESM 2.0. *Journal of Advances in Modeling Earth Systems*, **13** (12), e2021MS002585, <https://doi.org/10.1029/2021MS002585>, URL <https://onlinelibrary.wiley.com/doi/abs/10.1029/2021MS002585>, _eprint: <https://onlinelibrary.wiley.com/doi/pdf/10.1029/2021MS002585>.

Zängl, G., D. Reinert, P. Rípodas, and M. Baldauf, 2015: The ICON (ICOsahedral Non-hydrostatic) modelling framework of DWD and MPI-M: Description of the non-hydrostatic dynamical core. *Quarterly Journal of the Royal Meteorological Society*, **141** (687), 563–579, <https://doi.org/10.1002/qj.2378>, URL <https://rmets.onlinelibrary.wiley.com/doi/full/10.1002/qj.2378>, publisher: John Wiley and Sons Ltd.